Global superscaling analysis of quasielastic electron scattering with relativistic effective mass

J. E. Amaro,[*] V. L. Martinez-Consentino,[†] E. Ruiz Arriola,[‡] and I. Ruiz Simo[§]
Departamento de Física Atómica, Molecular y Nuclear and Instituto Carlos I de Física Teórica y Computacional Universidad de Granada, E-18071 Granada, Spain

(Received 26 June 2018; published 28 August 2018)

We present a global analysis of the inclusive quasielastic electron scattering data with a superscaling approach with relativistic effective mass. The SuSAM* model exploits the approximation of factorization of the scaling function $f^*(\psi^*)$ out of the cross section under quasifree conditions. Our approach is based on the relativistic mean field theory of nuclear matter where a relativistic effective mass for the nucleon encodes the dynamics of nucleons moving in presence of scalar and vector potentials. Both the scaling variable ψ^* and the single nucleon cross sections include the effective mass as a parameter to be fitted to the data alongside the Fermi momentum k_F. Several methods to extract the scaling function and its uncertainty from the data are proposed and compared. The model predictions for the quasielastic cross section and the theoretical error bands are presented and discussed for nuclei along the periodic table from $A = 2$ to $A = 238$: ^{2}H, ^{3}H, ^{3}He, ^{4}He, ^{12}C, ^{6}Li, ^{9}Be, ^{24}Mg, ^{59}Ni, ^{89}Y, ^{119}Sn, ^{181}Ta, ^{186}W, ^{197}Au, ^{16}O, ^{27}Al, ^{40}Ca, ^{48}Ca, ^{56}Fe, ^{208}Pb, and ^{238}U. We find that more than 9 000 of the total $\approx$ 20 000 data fall within the quasielastic theoretical bands. Predictions for ^{48}Ti and ^{40}Ar are also provided for the kinematics of interest to neutrino experiments.

DOI: 10.1103/PhysRevC.98.024627

I. INTRODUCTION

Inclusive electron scattering is a powerful tool to study the quasielastic response of nuclei, which arises in the region of energy-momentum transfer (ω, q), dominated by direct knockout of bound nucleons. These reactions have experienced a revival due to the recent neutrino oscillation experiments, which need precise modeling of neutrino scattering from nuclei at intermediate energies [1–5]. The recent measurements of CC neutrino and antineutrino cross sections [6–12] have allowed to test the current models as applied to neutrino scattering. Systematic differences between the theoretical predictions of the neutrino and antineutrino data from different groups have been found [13–21]. Work is in progress to conciliate the models, trying to find the origin of their differences and to reduce the systematic errors.

However, in the neutrino experiments the incident energy cannot be fixed, and the measurements are cross-section averages weighted by some known neutrino flux. Therefore, the detailed differences between models of the quasielastic response of nuclei should be further investigated through the corresponding predictions for (e, e') data. Despite the progress achieved with nuclear models based on first principles [22], the nuclear shell model [23], or the spectral function theory [24,25], the high energies and momenta for the kinematics of interest $q \approx 1$ GeV/c require important relativistic corrections [26,27] that are not easy to implement in models of finite nuclei. Other fundamental requirements like gauge invariance or off-shell extrapolations of the currents can also generate theoretical ambiguities and discrepancies in the results. Moreover, reaction mechanisms modifying the impulse approximation, such as final-state interactions, short-range correlations, meson-exchange currents, pion emission, and inelastic excitations, make it difficult to construct a sensible model providing a complete description of the whole set of (e, e') data at the full range of kinematics.

Relativity not only plays a role in the kinematics and in the current operator, but also in the dynamics. In a fully relativistic mean field model [28] the scalar and vector relativistic potentials enlarge the lower components of the (Dirac) nucleon wave functions in the medium [29], and this produces a notable enhancement of the transverse response function. This genuine relativistic dynamical effect does not appear in semi-relativistic approximations based in two-components (Pauli) spinors [27]. Thus, the so-called enhancement of the transverse response [15,30] cannot be attributed fully to multinucleon processes with meson-exchange currents but also, and significantly, to relativity. This shows that the separation of 1p-1h and 2p-2h channels in inclusive scattering is in fact ambiguous and model-dependent. Another example of ambiguity due to the medium in the channel expansion appears is the Δ peak, which usually is attributed to pion emission with an intermediate Δ resonance, but the Δ is dressed in the medium and part of its width is produced by decay into the 2p-1h channel [31–33] without pions.

Scaling studies are promising phenomenological alternatives to study the nuclear response [34]. In the superscaling approach (SuSA) [35–38] the longitudinal response function is divided by a single-nucleon structure function and plotted against a scaling variable ψ', which is proportional to the

[*]amaro@ugr.es
[†]victormc@ugr.es
[‡]earriola@ugr.es
[§]ruizsig@ugr.es

minimum initial momentum of the nucleons ejected by given momentum and energy transfer (q, ω). The scaling variable ψ' is made dimensionless by using units of the Fermi momentum k_F and takes into account the separation energy by subtraction of a parameter ϵ_B to the energy transfer ω. The data, scaled in this way for different kinematics and nuclear species, are found to collapse into a universal longitudinal scaling function $f_L(\psi')$. The corresponding transverse scaling function $f_T(\psi')$ could not be directly extracted from the data because the transverse response in contaminated from non-quasielastic processes explicitly breaking scaling such as pion emission and multinucleon emission originated mainly by meson exchange currents. In the SuSA approach it was assumed that $f_T = f_L$ [38] and this allowed to construct a simple model to predict neutrino cross sections from the (e, e') data.

Even with the appropriate relativistic corrections in the kinematics and currents [27] most of the nuclear models give $f_T \simeq f_L$ in the impulse approximation. Therefore, these models—SuSA included—cannot describe the (e, e') data without additional transverse enhancement mechanisms. However, including relativity in the dynamics one naturally finds an enhancement $f_T > f_L$, going into the right direction for the conciliation with data. This is the case of the relativistic mean field (RMF) model of finite nuclei [28], which is based on the Dirac-Hartree theory of Ref. [39].

The key ingredient to perform the upgrade SuSA-v2 [40] was to include nuclear effects theoretically-inspired by the RMF. SuSA-v2 uses an enhanced transverse scaling function f_T different from f_L. The new transverse scaling function was fitted to (e, e') cross-section data in a model including also 2p-2h MEC and inelastic contributions [41]. An additional dependence of $f_T(\psi')$ on the momentum transfer q was needed to reproduce the data. Therefore, the SuSA-v2 results violate scaling, although the model keeps the word "scaling" by tradition.

In recent work we have revisited the scaling approach by introducing a new scaling function $f^*(\psi^*)$ including dynamical relativistic effects [42–44] through the introduction of an effective mass into its definition. The resulting superscaling approach with relativistic effective mass (SuSAM*) model describes a large amount of the electron data lying inside a phenomenological quasielastic band, and it has been extended recently to the neutrino and antineutrino sector [45] with success and a fair agreement with the data. SuSAM* was first developed from the set of ^{12}C data [42,43] and later applied to other nuclei in Ref. [44].

The novel point of view of SuSAM* stems from the observation that a large subset of (e, e') data collapse into a thick band, which can be parameterized as a QE central value $f^*(\psi^*)$ plus or minus a theoretical uncertainty. This phenomenological QE scaling band emerges as the set of selected data which can be considered approximately quasielastic except for interaction effects which break scaling just by a little amount. The success to describe the cross-section data with only one scaling function is due to the proved good properties of the relativistic mean field, which already includes by construction the transverse response enhancement [46–48]. Moreover, the new phenomenological scaling function approximately encloses the universal scaling function of the relativistic Fermi gas,

$$f_{\rm RFG}(\psi^*) = \tfrac{3}{4}(1-\psi^{*2})\theta(1-\psi^{*2}). \tag{1}$$

This is so because the mean field theory of nuclear matter already provides a reasonable description of the quasielastic response function [46–48]. The phenomenological SuSAM* scaling function differs from this parabolic shape and it can be parameterized as a sum of two Gaussians. An additional advantage of the SuSAM* is that it keeps gauge invariance. The original SuSA violates this fundamental symmetry because it introduces an energy shift to account for separation energy, and hence initial and final states have a different mass, presumably modifying the vertex function. In our case the energy shift is accounted for by the effective mass, typically of $M^* = m^*_M/m_N \approx 0.8$ for medium-size nuclei.

The goal of the present work is twofold. First, to perform a global simultaneous fit of the SuSAM* parameters to all the available data on the (e, e') database compiled in Refs. [49–51]. Second, to present in a comprehensive way the model description of the cross section for all the nuclei included in the fit. We also analyze in more detail several nuclei and compare the various prescriptions used to extract the scaling function. Finally, we examine the predictions of our model to new (e, e') measurements for the nuclei ^{48}Ti [52] and ^{40}Ar, at present of interest for current neutrino experiments.

The scheme of the paper is as follows. In Sec. II we present the formalism for the (e, e') cross section. In Sec. III we present the results for the SuSAM* scaling function. In Sec. IV we present the predictions for the cross sections of the different nuclei. In Sec. V we draw our conclusions.

II. FORMALISM

Here we summarize, for completeness and to fix our notation, the general formalism of quasielastic electron scattering and the relativistic mean field model of nuclear matter [42]. We assume that an incident electron transfers momentum $\mathbf{q}$ and energy ω to the nucleus, scattering to an angle θ. The four-momentum transfer is denoted as $Q^2 = \omega^2 - q^2 < 0$. The quasielastic cross section is written in the plane wave Born approximation with one-photon-exchange in terms of the longitudinal and transverse response functions as

$$\frac{d\sigma}{d\Omega' d\epsilon'} = \sigma_{\rm Mott}(v_L R_L + v_T R_T). \tag{2}$$

Here, $\sigma_{\rm Mott}$ is the Mott cross section, and the kinematic factors v_L, v_T are defined by

$$v_L = \frac{Q^4}{q^4}, \tag{3}$$

$$v_T = \tan^2\frac{\theta}{2} - \frac{Q^2}{2q^2}. \tag{4}$$

Finally, $R_L(q, \omega)$ and $R_T(q, \omega)$ are the nuclear longitudinal and transverse response functions, respectively. The L and T responses are computed starting with the RMF in nuclear matter [53]. We consider one-particle one-hole (1p-1h) excitations in the nuclear medium produced by one-body electromagnetic current operator, such that the initial and final nucleons have

TABLE I. Parameters of the central value of the phenomenological scaling function, $f^*(\psi^*)$, and those of the lower and upper boundaries (min and max, respectively) of the bands. Band A correspond to the ^{12}C fit of Ref. [43], Band B correspond to the 12-nuclei fit of Ref. [44], and band C is the global fit performed in this work.

		a_1	a_2	a_3	b_1	b_2	b_3	c_1	c_2
	Central	− 0.0465	0.469	0.633	0.707	1.073	0.202	—	—
Band A	Min	− 0.0270	0.442	0.598	0.967	0.705	0.149	—	—
	Max	− 0.0779	0.561	0.760	0.965	1.279	0.200	—	—
	Central	− 0.1335	0.4319	1.3885	0.5741	0.6539	0.6083	0.3405	2.2947
Band B	Min	0.3075	0.6898	0.4115	− 0.0647	0.3145	0.3267	− 0.8362	0.0295
	Max	− 7.0719	2.4644	38.58	− 7.0724	2.4595	38.58	− 0.2613	0.2410
	Central	− 0.0537	0.5051	0.6055	0.7258	1.0102	0.2306	− 0.9765	0.1716
Band C	Min	− 0.0435	0.4245	0.4940	0.5129	0.7360	0.2346	− 0.8549	0.0337
	Max	− 0.1192	0.4955	1.1504	0.7001	1.0939	0.3992	− 1.0058	1.9235

the *same* effective mass m_N^*. Thus, the initial nucleon has energy $E = \sqrt{\mathbf{p}^2 + m_N^{*2}}$ in the mean field, with p below the Fermi momentum, $p < k_F$. The final momentum of the nucleon is $\mathbf{p}' = \mathbf{p} + \mathbf{q}$, and its corresponding energy is $E' = \sqrt{\mathbf{p}'^2 + m_N^{*2}}$. Pauli blocking implies $p' > k_F$.

The nuclear response functions can be written in the factorized form,

$$R_K = r_K f^*(\psi^*), \tag{5}$$

for $K = L, T$. Here, r_L and r_T are the single-nucleon contributions to the response functions, averaged over the Fermi motion given below. $f^*(\psi^*)$ is the scaling function, given by Eq. (1). It depends only on the scaling variable ψ^*, which is defined as follows.

First, it is convenient to introduce the dimensionless variables

$$\lambda = \omega/2m_N^*, \tag{6}$$

$$\kappa = q/2m_N^*, \tag{7}$$

$$\tau = \kappa^2 - \lambda^2, \tag{8}$$

$$\eta_F = k_F/m_N^*, \tag{9}$$

$$\xi_F = \sqrt{1 + \eta_F^2} - 1, \tag{10}$$

$$\epsilon_F = \sqrt{1 + \eta_F^2}. \tag{11}$$

TABLE II. Values of the parameters M^* and k_F (in MeV/c) obtained from the different fits to the scaling band, the total number of data $N_{\rm tot}$, the number $N_{\rm QE}$ of quasielastic points, and the χ^2 divided by the number $N'_{\rm QE}$ of quasielastic points (with $-1 < \psi^* < 1$ in the case of ^{2}H and ^{3}He).

	Visual fit		No. points fit		χ^2 fit		Global fit		No. points		
Nucleus	k_F [MeV/c]	M^*	k_F	M^*	k_F	M^*	k_F	M^*	$N_{\rm QE}$	$N_{\rm tot}$	$\chi^2/N'_{\rm QE}$
^{2}H	80	1.00	88	0.99	82	1.00	81	0.99	426	2135	0.372
^{3}H	120	0.97	142	0.99	136	0.98	126	0.97	139	540	0.414
^{3}He	140	0.95	147	0.96	130	0.98	130	0.96	794	2472	0.565
^{4}He	160	0.90	180	0.89	180	0.86	159	0.87	803	2718	0.699
^{6}Li	165	0.80	—	—	175	0.77	164	0.80	23	165	0.18
^{9}Be	185	0.80	—	—	202	0.85	184	0.80	16	390	0.07
^{12}C	225	0.80	226	0.82	217	0.80	212	0.83	660	2883	0.697
^{16}O	230	0.80	259	0.84	250	0.79	228	0.80	48	126	0.999
^{24}Mg	235	0.75	—	—	238	0.65	235	0.75	23	34	0.313
^{27}Al	236	0.80	258	0.78	249	0.80	233	0.80	75	628	0.499
^{40}Ca	240	0.73	250	0.73	236	0.71	229	0.74	616	1339	0.76
^{48}Ca	247	0.73	242	0.75	237	0.71	230	0.75	728	1227	0.672
^{56}Fe	238	0.70	240	0.79	241	0.70	240	0.72	485	2429	1.20
^{59}Ni	235	0.67	—	—	238	0.65	234	0.68	27	37	0.09
^{89}Y	235	0.65	—	—	224	0.64	233	0.65	27	37	0.17
^{119}Sn	235	0.65	—	—	232	0.64	236	0.66	24	34	0.204
^{181}Ta	235	0.65	—	—	232	0.64	236	0.66	24	33	0.115
^{186}W	230	0.77	—	—	226	0.76	231	0.80	45	184	0.6
^{197}Au	240	0.75	—	—	238	0.78	235	0.74	30	96	0.237
^{208}Pb	237	0.65	239	0.64	233	0.56	232	0.63	818	1714	1.223
^{238}U	259	0.65	219	0.59	219	0.51	255	0.65	193	420	1.74

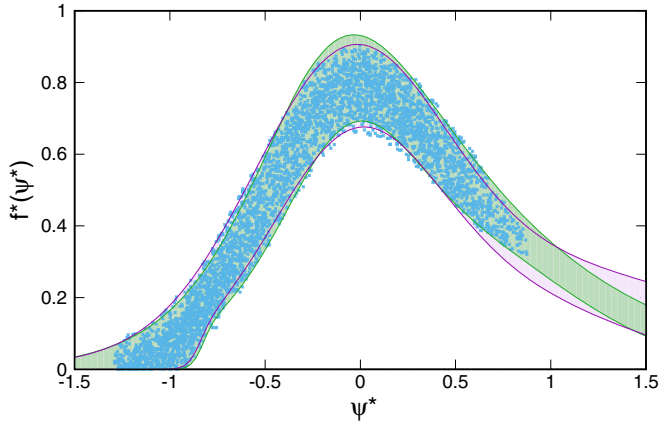

FIG. 1. Phenomenological scaling function bands compared to the (e, e') data scaled with the best parameters of the global fit and selected with the density criterion. The corresponding scaling function band C (in pink) is compared to the band B of Ref. [44] (in green). The data are selected from Refs. [49–51].

Note that in the SuSA formalism these variables are defined dividing by the nucleon mass m_N instead of m_N^* [34].

Then, one computes the minimum energy for the initial nucleon that is allowed to absorb the energy and momentum transfer (q, ω). From energy and momentum conservation, in units of m_N^* it is given by

$$\epsilon_0 = \mathrm{Max}\left\{\kappa\sqrt{1+\frac{1}{\tau}} - \lambda, \epsilon_F - 2\lambda\right\}. \tag{12}$$

We can finally write the definition of the scaling variable as

$$\psi^* = \sqrt{\frac{\epsilon_0 - 1}{\epsilon_F - 1}}\,\mathrm{sgn}(\lambda - \tau). \tag{13}$$

The sign convention is such that ψ^* is negative to the left of the quasielastic peak (defined by $\lambda = \tau$) and positive on the right side.

The nucleonic contributions to the responses are

$$r_K = \frac{\xi_F}{m_N^* \eta_F^3 \kappa}\left(Z U_K^p + N U_K^n\right) \tag{14}$$

for Z protons and N neutrons. The single-nucleon response functions longitudinal and transverse, U_L, U_T are computed from the matrix elements of the electromagnetic current operator.

In this work we use the CC2 prescription of the electromagnetic current operator [54]

$$J^\mu_{s's} = \bar{u}_{s'}(\mathbf{p}')\left[F_1\gamma^\mu + F_2 i\sigma^{\mu\nu}\frac{Q_\nu}{2m_N}\right]u_s(\mathbf{p}), \tag{15}$$

where F_i are the Pauli form factors of the nucleon, and the spinors contain the effective mass instead of the bare nucleon mass. Therefore, the above matrix element differs from the bare nucleon result with $m_N^* = m_N$. As a consequence the electric and magnetic form factors are modified in the medium according to [42,53]

$$G_E^* = F_1 - \tau\frac{m_N^*}{m_N}F_2, \tag{16}$$

$$G_M^* = F_1 + \frac{m_N^*}{m_N}F_2. \tag{17}$$

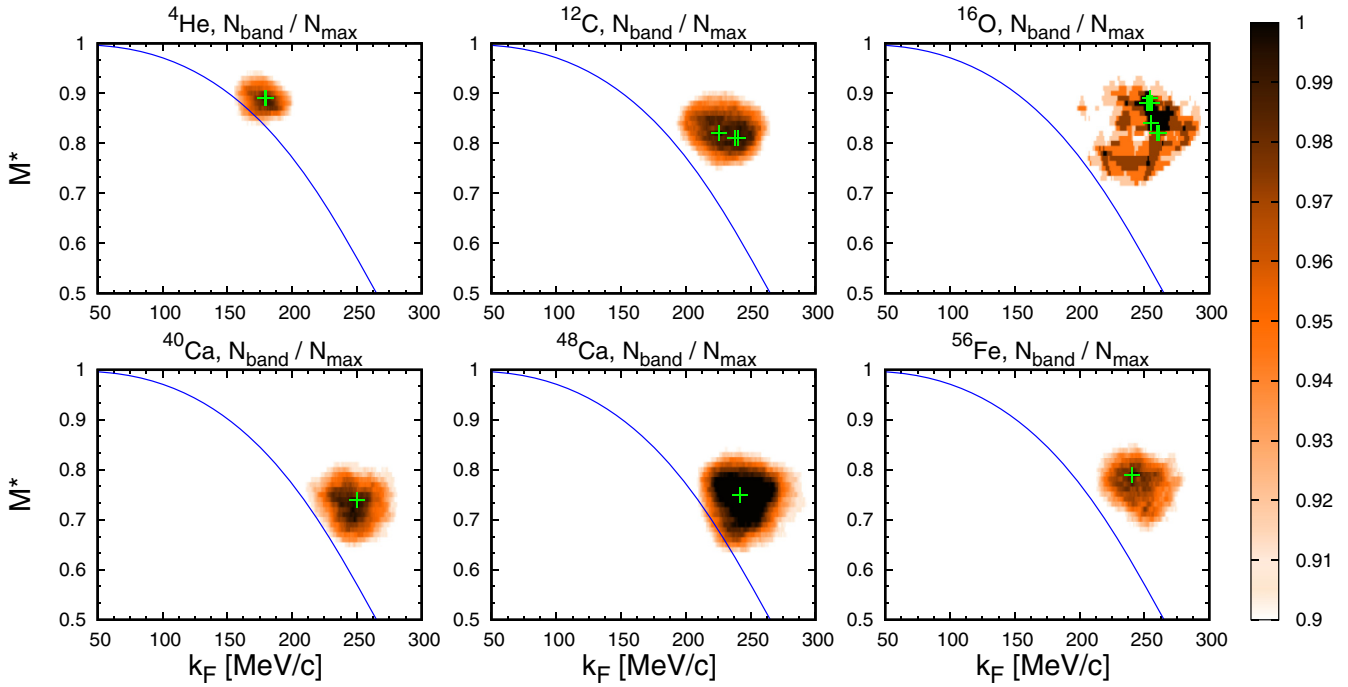

FIG. 2. Color maps of the number, N, of QE data inside the phenomenological band divided by $N_{\max}$, as a function of the effective mass M^* and Fermi momentum k_F for different nuclei. The σ-ω model of Ref. [47] is shown as comparison.

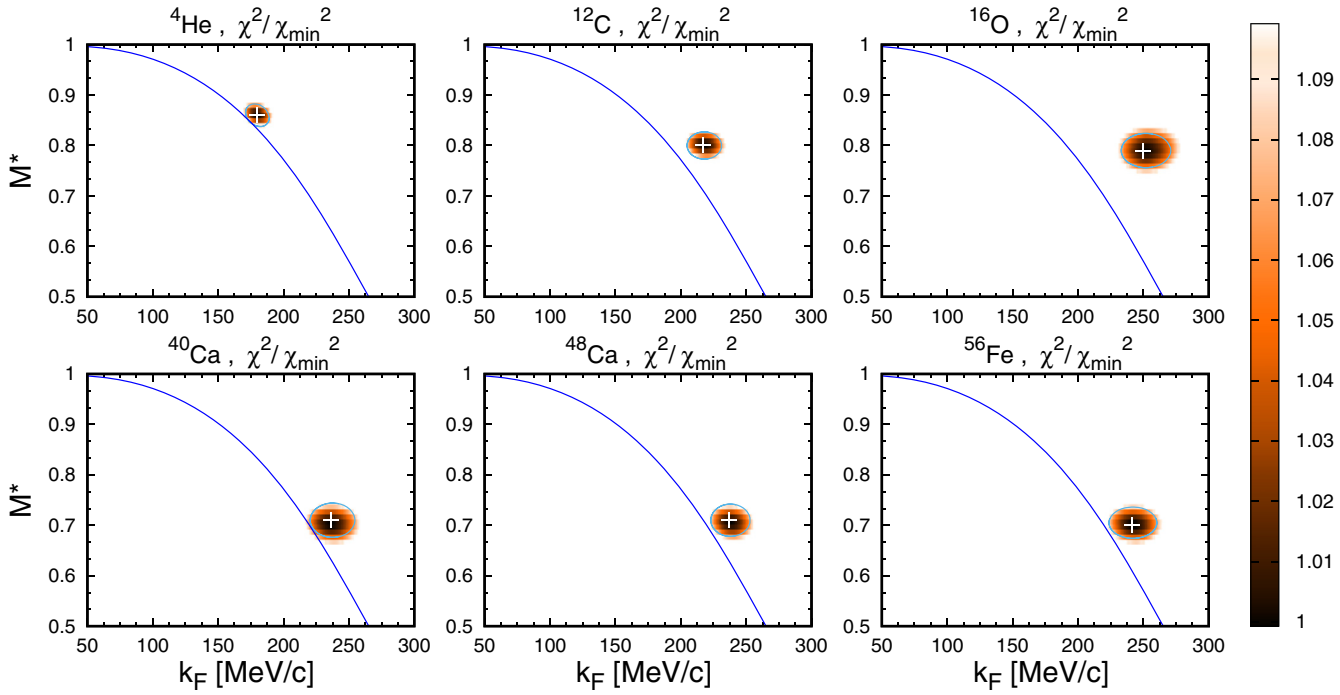

FIG. 3. Color maps of the χ^2 of the QE data with the phenomenological band, divided by $\chi^2_{\min}$, as a function of the effective mass M^* and Fermi momentum k_F for different nuclei. The region with χ^2 above 10% of the minimum is shown in white. The region with χ^2 below 10% of the minimum is fitted by a ellipse. The σ-ω model of Ref. [47] is shown as comparison.

For the free Dirac and Pauli form factors, F_1 and F_2, we use the Galster parametrization [55].

Using the above definitions, the single-nucleon response functions are given by

$$U_L = \frac{\kappa^2}{\tau}\left[(G_E^*)^2 + \frac{(G_E^*)^2 + \tau(G_M^*)^2}{1+\tau}\Delta\right], \tag{18}$$

$$U_T = 2\tau(G_M^*)^2 + \frac{(G_E^*)^2 + \tau(G_M^*)^2}{1+\tau}\Delta. \tag{19}$$

Here we use the quantity Δ defined by

$$\Delta = \frac{\tau}{\kappa^2}\xi_F(1-\psi^{*2})\left[\kappa\sqrt{1+\frac{1}{\tau}} + \frac{\xi_F}{3}(1-\psi^{*2})\right]. \tag{20}$$

This is usually a small correction around the QE peak $-1 < \psi^* < 1$, because it is proportional to the small quantity ξ_F.

III. THE SUSAM* APPROACH

In the SuSAM* approach the cross section is computed by using Eqs. (2) and (5) but replacing the RFG scaling function by a phenomenological one $f^*(\psi^*)$ extracted from the experimental data.

This can be done in several ways with a careful analysis of the scaling properties of (e, e') cross-section data. We carried out such analyses in Refs. [42–44].

In this work we extend those studies starting with ≈20 000 experimental (e, e') cross-section data for 21 nuclei: ^{2}H, ^{3}H, ^{3}He, ^{4}He, ^{12}C, ^{6}Li, ^{9}Be, ^{24}Mg, ^{59}Ni, ^{89}Y, ^{119}Sn, ^{181}Ta, ^{186}W, ^{197}Au, ^{16}O, ^{27}Al, ^{40}Ca, ^{48}Ca, ^{56}Fe, ^{208}Pb, and ^{238}U. For every datum we compute the corresponding experimental scaling function $f^*_{\rm exp}$ by dividing the experimental cross section by the single nucleon function introduced in the last section:

$$f^*_{\rm exp} = \frac{\left(\frac{d\sigma}{d\Omega' d\epsilon'}\right)_{\rm exp}}{\sigma_{\rm Mott}(v_L r_L + v_T r_T)}. \tag{21}$$

From the experimental kinematics we also compute the corresponding value of the scaling variable ψ^*. When we plot f^* versus ψ^* one observes that a subset of data are concentrated around a band, but the scaling is not perfect. One then tries to change the values of the parameters M^* and k_F up to find the best scaling possible.

The analysis has been developed in several stages that we describe next. For completeness, we summarize with some

TABLE III. Parameters of the 10% confidence ellipses of the χ^2 fits.

Nuclei	$(k_F)_c$	M^*_c	a	b	θ
^{2}H	82.5	0.994	0.006	0.02	105
^{3}H	136	0.98	0.016	0.014	145
^{3}He	125.5	0.988	0.010	0.038	90
^{4}He	180	0.86	0.031	0.021	20
^{12}C	218	0.8	0.027	0.044	90
^{16}O	252	0.79	0.034	0.063	90
^{27}Al	249.5	0.795	0.029	0.05	95
^{40}Ca	237.5	0.71	0.034	0.057	90
^{48}Ca	238	0.71	0.032	0.05	90
^{56}Fe	242	0.705	0.061	0.031	0
^{208}Pb	233	0.56	0.035	0.062	90
^{238}U	221	0.52	0.027	0.064	90

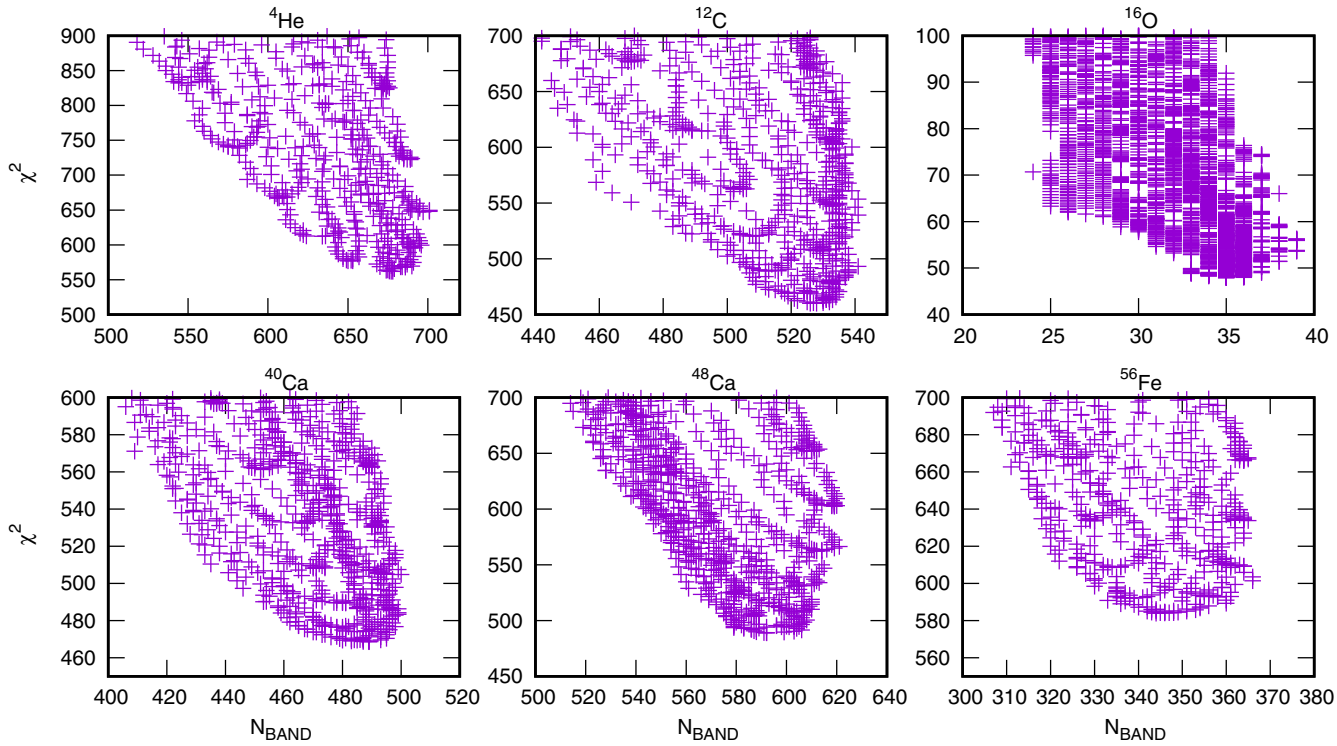

FIG. 4. Correlation plot of the χ^2 values versus the number of points inside the band $N_{\rm band}$ for different values of k_F and M^* around the region where χ^2 is minimum and $N_{\rm band}$ reaches its maximum, for six nuclei.

details what we did in the past works [42–44], while we will explain in depth those aspects of the fits that were not accounted for previously. The goals of this section are:

(1) to show the self consistency of the extraction of the scaling function,
(2) to check that the different methods produce similar results for the SuSAM* parameters, and
(3) to perform a global fit of the parameters and scaling function simultaneously.

A. The scaling function

We started with the ^{12}C data, by tuning the parameters M^* and k_F until one finds the best scaling possible. This was reached in Ref. [42] for $M^* = 0.8$ and $k_F = 225$ MeV/c. By applying a density criterion, a data cloud around the RFG scaling function was selected. According with the criterion we selected those scaled data surrounded by more than 25 data inside a circle of radius $r = 0.1$ in the $f^*(\psi^*)$ graph. These selected data defined a "QE" region as a thick band which we parameterized as a combination of two Gaussian functions [43]:

$$f^*(\psi^*) = a_3 e^{-(\psi^*-a_1)^2/(2a_2^2)} + b_3 e^{-(\psi^*-b_1)^2/(2b_2^2)}. \quad (22)$$

The parameters of this band A are given in Table I.

Starting with band A we applied in Ref. [44] several methods to obtain the relativistic effective mass and the Fermi momentum of all the nuclei from the periodic table, for which (e, e') data existed in our data base, taken from Refs. [49,50]. With these values of (k_F, M^*) parameters we verified that all these nuclei approximately scale similarly to the ^{12}C ones. These parameters are shown in columns 2–7 of Table II. For this work we have revised the analysis of Ref. [44] for the nuclei ^{2}H and ^{3}He, which have been updated in Table II.

The procedure required to obtain first k_F and M^* for all the nuclei from a visual fit (columns 2–3 of Table II), providing a good qualitative scaling of the experimental data. With these parameters we scaled the data for the twelve main nuclei of the data base. Then, we proceeded to a more precise determination of the phenomenological scaling function by discarding those kinematics where the energy transfer at the QE peak is lower than ≈80–100 MeV, and also those of high energy were the QE peak is indistinguishable due to inelastic dominance.

With this set of data a density criterion was newly applied, obtaining a new SuSAM* phenomenological band. In Ref. [44] that scaling band was parameterized as the sum of two Gaussians, modified to improve the low energy region by applying a Fermi function:

$$f^*(\psi^*) = \frac{a_3 e^{-(\psi^*-a_1)^2/(2a_2^2)} + b_3 e^{-(\psi^*-b_1)^2/(2b_2^2)}}{1 + e^{-\frac{\psi^*-c_1}{c_2}}}. \quad (23)$$

The parameters of this scaling function are given in Table I. They are labeled as "band B." We provide the parameters of the lower (min) and upper (max) limits of the boundary, defining the uncertainty band. The central parameters correspond to the best fit to the selected data. Band B is shown as the green band in Fig. 1. This is compared to the band C that is obtained in the global fit explained below. Both bands are similar around the quasielastic region, and therefore they are interchangeable

in cross-section calculations. Band B is the one used in the SuSAM* model of the next section to compute the QE cross sections of nuclei.

Note that the scaling band shown in Fig. 1 is well defined only in the quasielastic region $-1 < \psi^* < 1$, while we cannot describe in detail the left tail of the cross section, corresponding to $\psi^* < -1$, and related to higher momentum components produced mainly by nucleon-nucleon short range correlations [56,57], which break M^*-scaling. A detailed study of this region is beyond of the scope of the present work.

B. The parameters k_F and M^*

We recall that band B was obtained in the last subsection from the scaling of data using a visual fit of the parameters k_F and M^*. For consistency it is pertinent to recompute those parameters with a more quantitative procedure, which we describe next. This will allow us also to obtain in return an estimate of their uncertainties. We can proceed in two different ways, which ultimately produce similar results for the parameters. The first is to maximize the number of points inside band B. The resulting parameters are given in columns 4 and 5 of Table II. The second method is to minimize a χ^2 function computed from the distances of the data to the center of the band for each nucleus, divided by the total error, taking into account the band width,

$$\chi^2 = \sum_{i=1}^{N'_{\rm QE}} \frac{(f^*(\psi_i^*)_{\rm exp} - f^*(\psi_i^*)_{\rm central})^2}{(\Delta f^*(\psi_i^*)_{\rm exp})^2 + (\Delta f^*(\psi_i^*)_{\rm th})^2}, \qquad (24)$$

where we have added in quadrature in the denominator the experimental and theoretical errors. The parameters resulting from minimization of this χ^2 are given in columns 6 and 7 of Table II.

Note that the number of points $N'_{\rm QE} = N_{\rm QE}$ included in the sum has been selected by leaving only the points that are clearly around the QE peak. These numbers of points are presented in the tenth column of Table II, together with the total number of points before the selection, which are shown in the eleventh column of the same table. The same data set used in the χ^2 minimization has been used in the maximization of the number of points inside the band. However, in the case of the nuclei ^{2}H and ^{3}He, revised in the present work, we have to include in the χ^2 only those points with $-1 < \psi^* < 1$ to obtain reasonable results. Therefore, for these two nuclei $N'_{\rm QE} < N_{\rm QE}$. For nine of the nuclei the number of experimental data is not large enough to obtain a reasonable fit, and those are hence not appearing in columns 4 and 5 of Table II.

The values of the parameters k_F and M^* obtained by these quantitative fits are similar between them and are also similar to the ones used in the visual fit from which band B was obtained. The agreement between the parameters obtained with different fits faithfully points to the steadiness and robustness of the present scaling approach for this purpose.

Besides, these methods allow us to compute estimations of the theoretical errors in the parameters. The procedure is illustrated in the color maps of Figs. 2 and 3 for six selected nuclei.

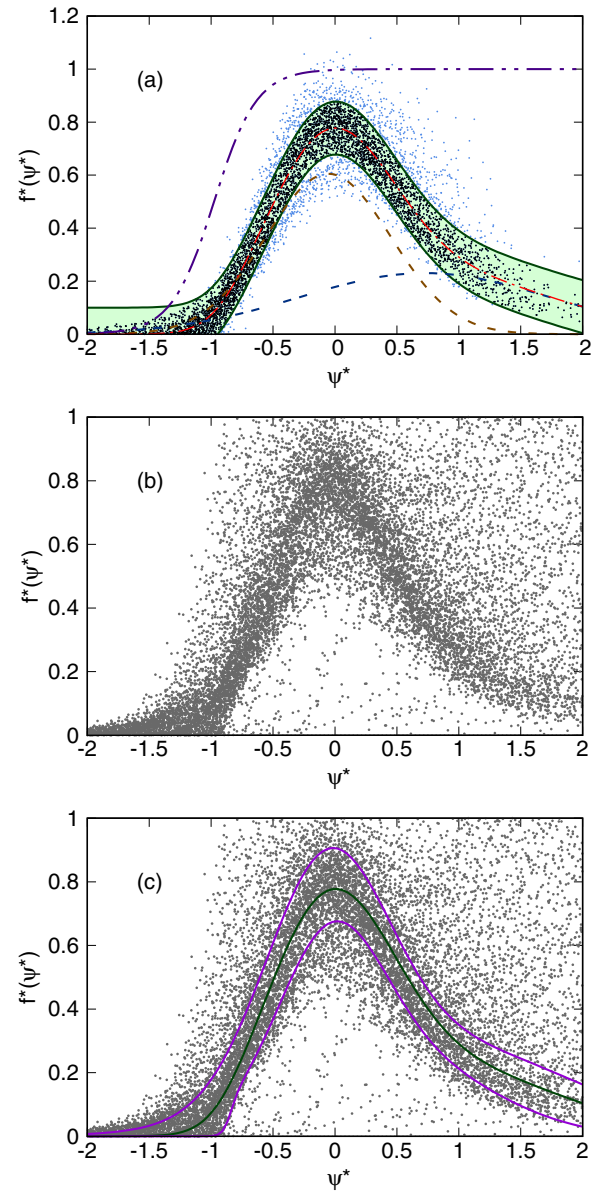

FIG. 5. Top panel: Data used in the global fit of the superscaling function. The fit is made by maximizing the number of data inside a band centered around a sample scaling function of width 0.1. In black the 4754 points falling inside the band after the fit. The central function (in red-dashed lines) is the sum of two Gaussians (shown in the figure in dashed and double-dashed lines) modified by a Fermi function (we show the denominator of the Fermi function in dash-double dotted line). Middle panel: Global set of (e, e') data scaled with the best parameters after the global fit. The scaling function appears as a dark shadow. Data are from Refs. [49–51]. Bottom panel: the same data compared to the parameterized band C.

In Fig. 2 we show the number of data inside band B divided by the maximum, $N_{\rm band}/N_{\rm max}$ as a function of M^* and k_F. We show the cloud where $N_{\rm band}/N_{\rm max}$ changes between 0.9 and 1. This means that changing the parameters around the position of the maximum inside the cloud the number of data that get out of band B is less than 10% of the maximum $N_{\rm max}$. Note that for some nuclei there is more than one maximum. In

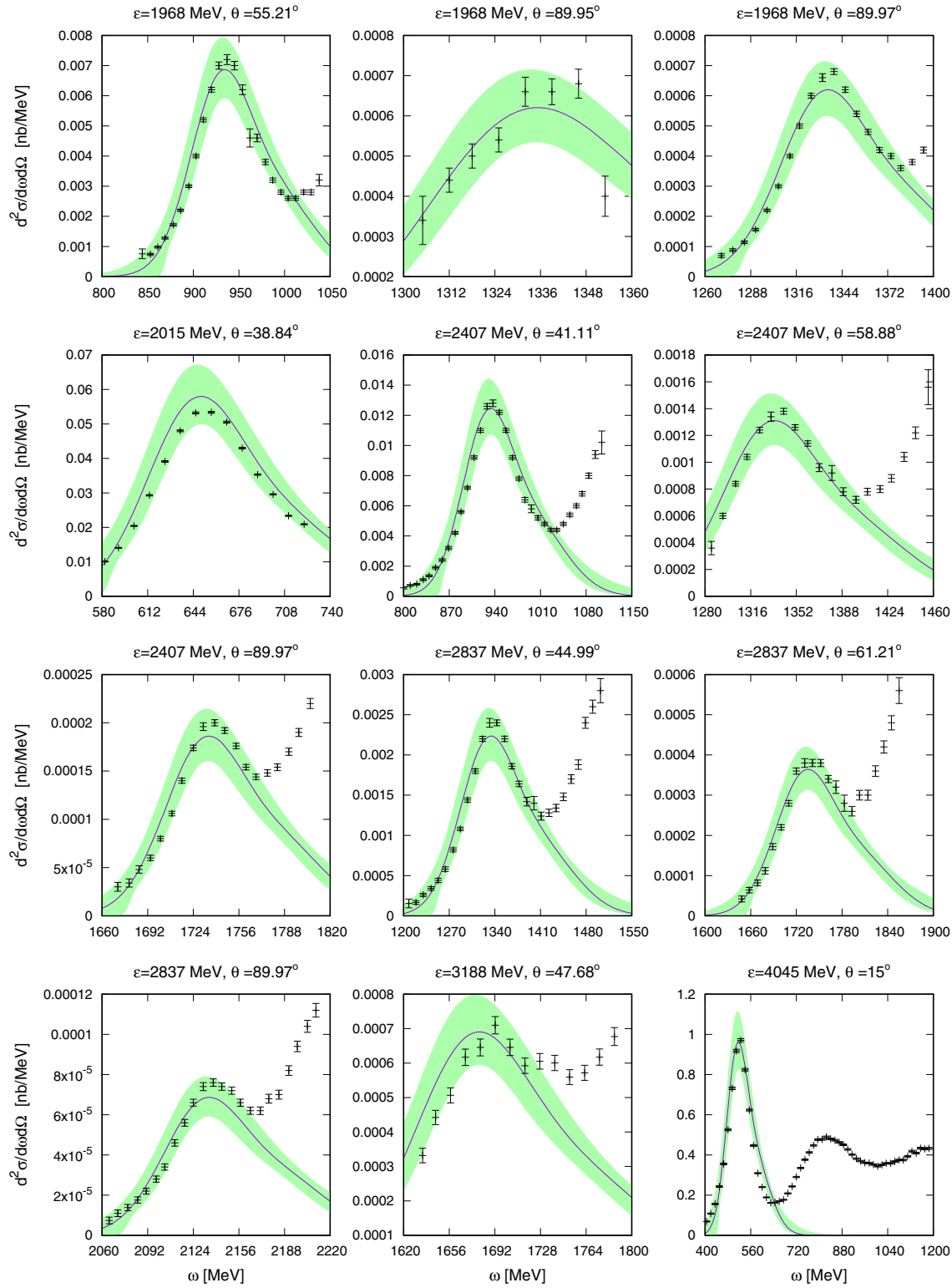

FIG. 6. Inclusive (e, e') cross-section data for ^{2}H for selected kinematics compared to the SuSAM* model as a function of energy transfer. Data are from Refs. [49–51].

that case we display in Table II the values closer to the $\sigma - \omega$ theory of the Walecka model [47], also shown in the figure. Note that maximizing the number of points inside the band is a discretized procedure and as consequence the shapes of the clouds deviate from a regular elliptic shape and this does not allow to parametrize the error in a systematic way.

The χ^2 minimization method shown in Fig. 3 is more appropriate to this end. In the figure we show the cloud

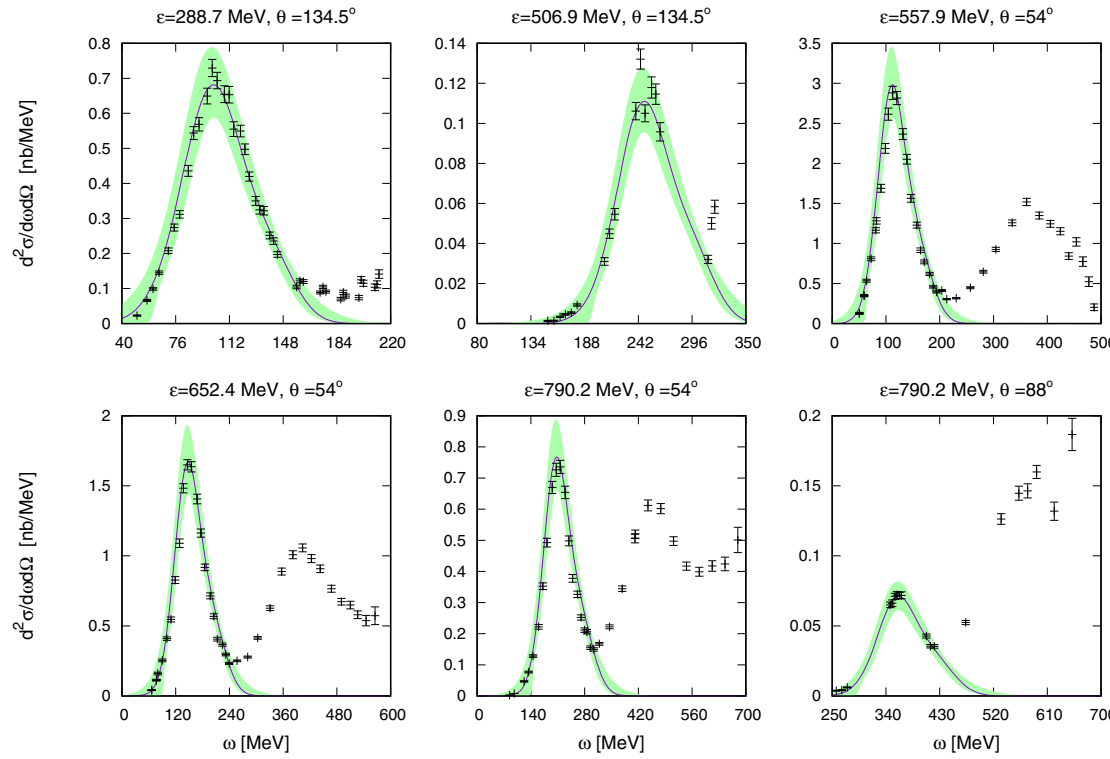

FIG. 7. Inclusive (e, e') cross-section data for ^{3}H for selected kinematics compared to the SuSAM* model as a function of energy transfer. Data are from Refs. [49–51].

in parameter space where the χ^2 values divided by the minimum $\chi^2_{\rm min}$ are in the range 1.0–1.1. The resulting 10% change clouds are more elliptic shaped and smaller than the clouds of Fig. 2. With these plots we are able to parametrize the cloud shapes using ellipses with three constants, a, b, θ:

$$k_F(s) = (k_F)_c + 300\text{MeV/c}[a\cos\theta\sin(s) + b\sin\theta\cos(s)], \tag{25}$$

$$M^*(s) = M^*_c - a\sin\theta\sin(s) + b\cos\theta\cos(s), \tag{26}$$

where s is the parameter of the ellipse. The ellipse parameters encode the errors in k_F, M^*(10% confidence interval) and they are given in Table III. Note that the centers of the ellipses are not exactly at the minimum χ^2 position because we are just interested in a rough estimation of the error and therefore we compute the ellipses with a finite variation of 10% in the χ^2 value.

Notice that the maximum of the number of points inside the band does not coincide with the minimum of χ^2. This is so because a set of points inside the band can occupy different positions resulting in different values of the χ^2. Thus, the value of χ^2 is not directly related to $N_{\rm band}$, although some correlations can be found between these two functions. The correlations between $N_{\rm band}$ and χ^2 depend on the particular nucleus, and the selected set of quasielastic data entering in the fit. This correlation is shown in Fig. 4 for six of the nuclei. In the figure we display the values of χ^2 versus $N_{\rm band}$ for different values of k_F, M^* around the extreme regions shown in Figs. 2 and 3. The correlation between χ^2 and $N_{\rm band}$ is stronger when $N_{\rm band}$ increases and χ^2 decreases. But we clearly observe that the maxima of $N_{\rm band}$ do not minimize χ^2, but they are close to do it.

C. The global fit

One of the goals of the present paper is to validate the universality of the scaling function by investigating the self consistency of the extraction method by an alternative way. To guarantee that the procedure is independent on a particular nuclear species, we have developed a global approach where the scaling function is not given *a priori*. Instead we fit at the same time all the parameters of the model, including the scaling function $f^*(\psi^*)$, and the Fermi momentum and effective mass of all the nuclei simultaneously. This global fit maximizes the number of QE data points, $f^*_{\rm exp}(\psi^*)$, falling inside a band around a scaling function, which we parametrize as a modified combination of Gaussians with eight parameters, as given in Eq. (23). We apply the downhill simplex method with fifty parameters (the Fermi momenta and effective mass of 21 nuclei, M^*, k_F, plus the eight parameters of the scaling function). The "scaling" band used in the fit has a constant width. It is defined by the limits $f^*(\psi^*) \pm 0.1$, i.e., for each datum, and for each set of parameters we accept the datum inside the band if $|f^*(\psi^*)_{\rm exp} - f^*(\psi^*)| < 0.1$. We start with "good" initial parameters obtained in one of the previous separate fits. The result of this fit is shown in the top panel of Fig. 5. The values of k_F and M^* are given in columns 8 and 9 of Table II. The parameters of the scaling function are given in Table I as the central part of band C.

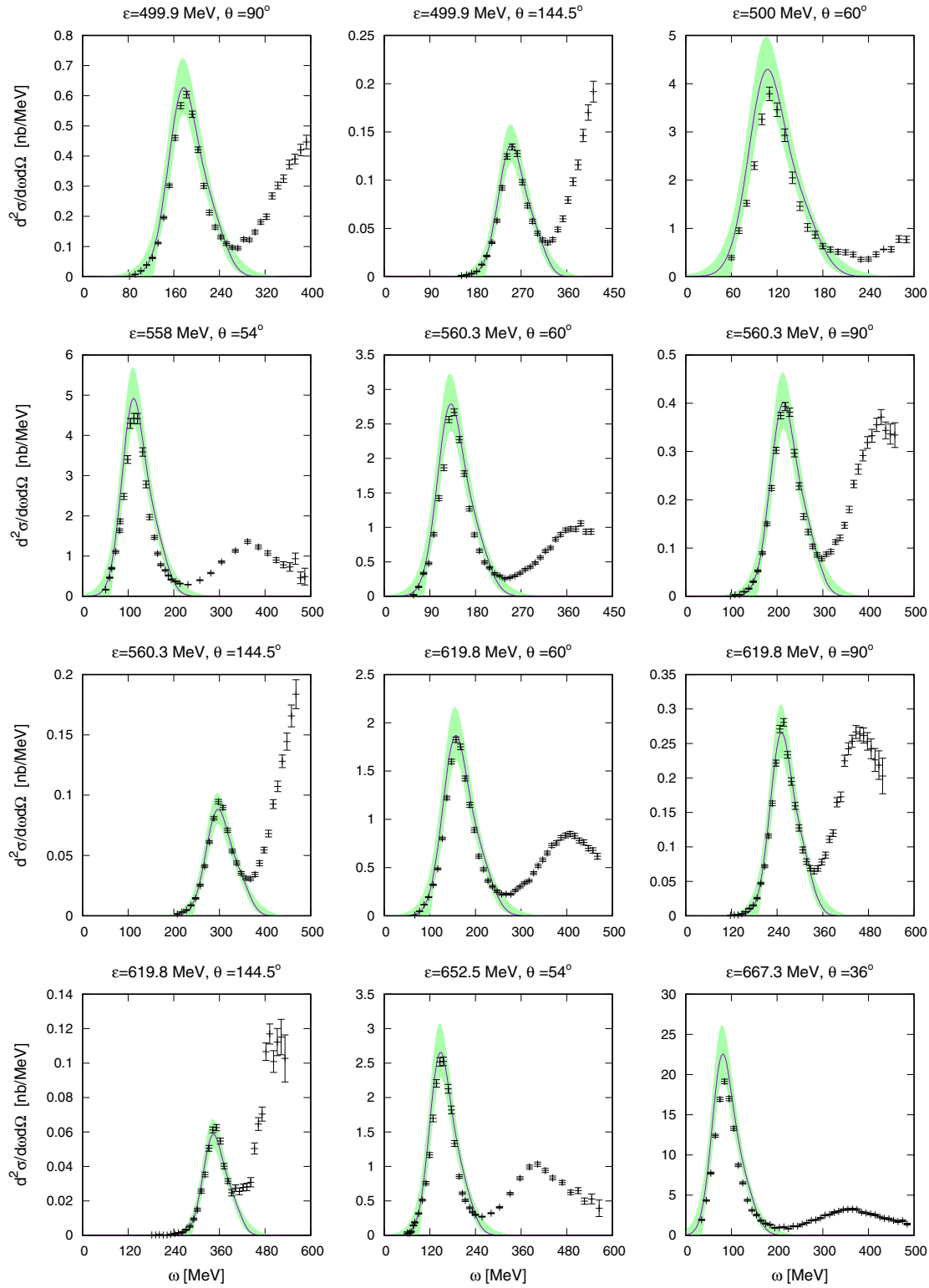

FIG. 8. Inclusive (e, e') cross-section data for ^{3}He for selected kinematics compared to the SuSAM* model as a function of energy transfer. Data are from Refs. [49–51].

This global fit only allows to obtain the central part of the scaling function but not the width of the band, which for the fit purposes has been fixed to a reasonable value chosen as ± 0.1, because in the previous analyses we have seen that this is the observed order of magnitude. To finish the extraction of the phenomenological band we therefore apply again a density criterion to select the true QE data to all the QE data scaled with the global parameters. We then obtain the set of true "scaling"

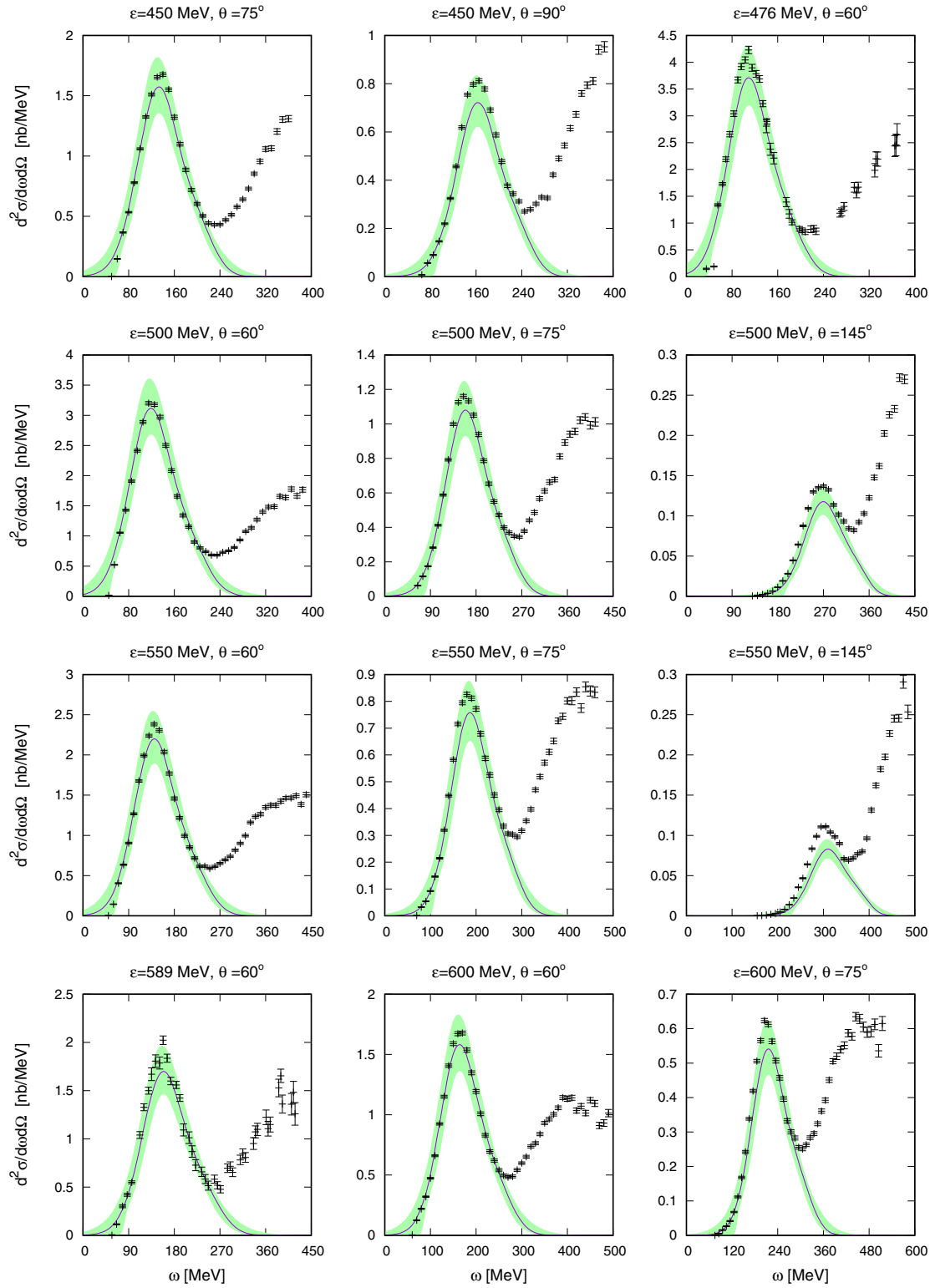

FIG. 9. Inclusive (e, e') cross-section data for ^{4}He for selected kinematics compared to the SuSAM* model as a function of energy transfer. Data are from Refs. [49–51].

QE data shown in Fig. 1. There are 4230 points in that figure, which are a 70% of all the points entering in the fit. These points clearly define a band which is again parameterized in the same way as before as in Eq. (23) and the parameters are given in Table I as band C. This band is shown in pink in Fig. 1. We can see that the result of this global fit is very similar

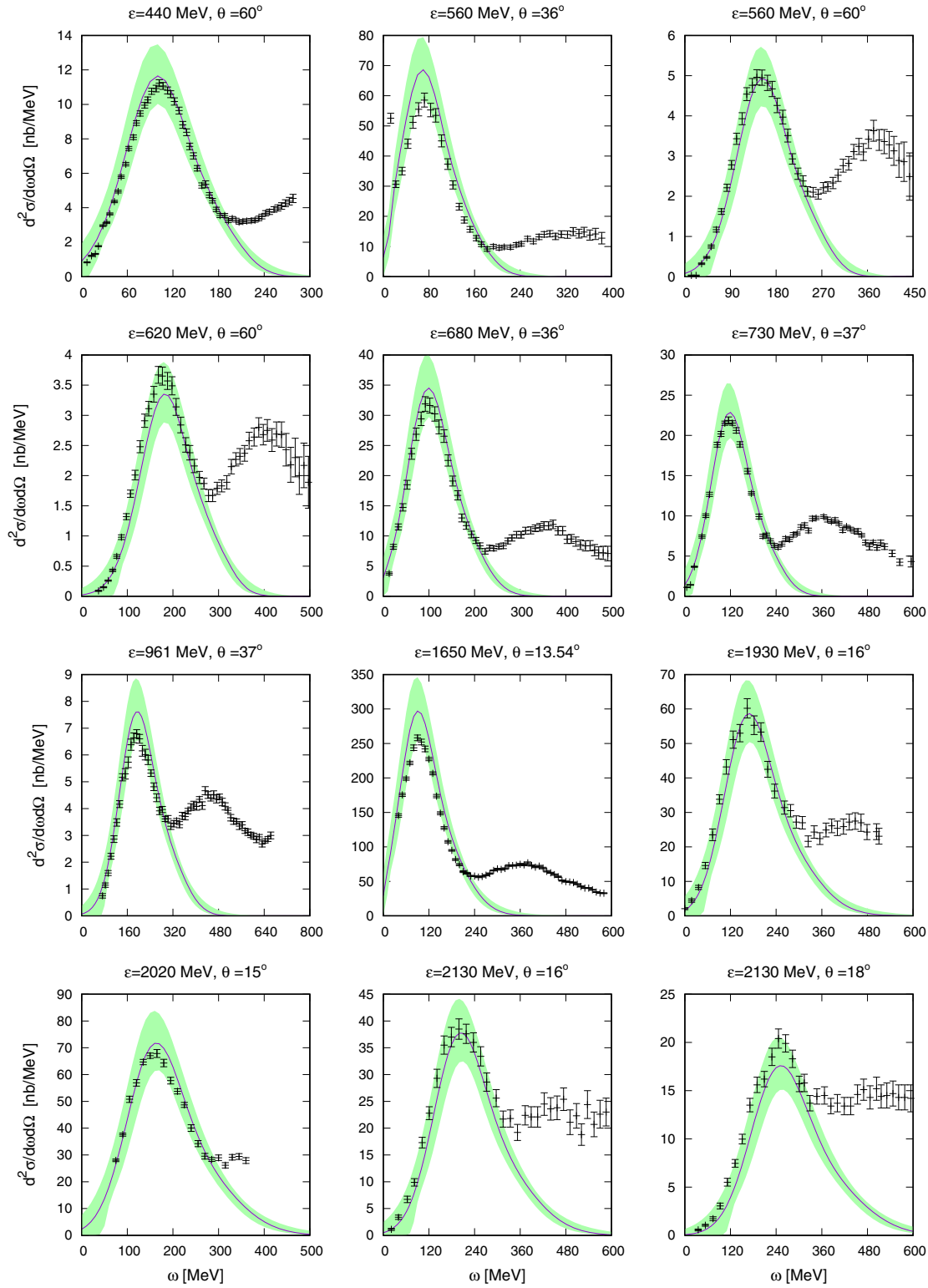

FIG. 10. Inclusive (e, e') cross-section data for ^{12}C for selected kinematics compared to the SuSAM* model as a function of energy transfer. Data are from Refs. [49–51].

to band B obtained by partial fits. These results enforce the self consistency hypothesis and the universality of the scaling function obtained.

To gain a perspective of the quality of the results we show in the middle panel of Fig. 5 all the data points (not only the QE ones) for all the nuclei scaled with the parameters of the global fit. Clearly a large fraction of data collapse into a dark shadow which resembles to our previously determined bands. In the bottom panel of Fig. 5 the same points are compared to the global scaling function and band C. In fact, the number of

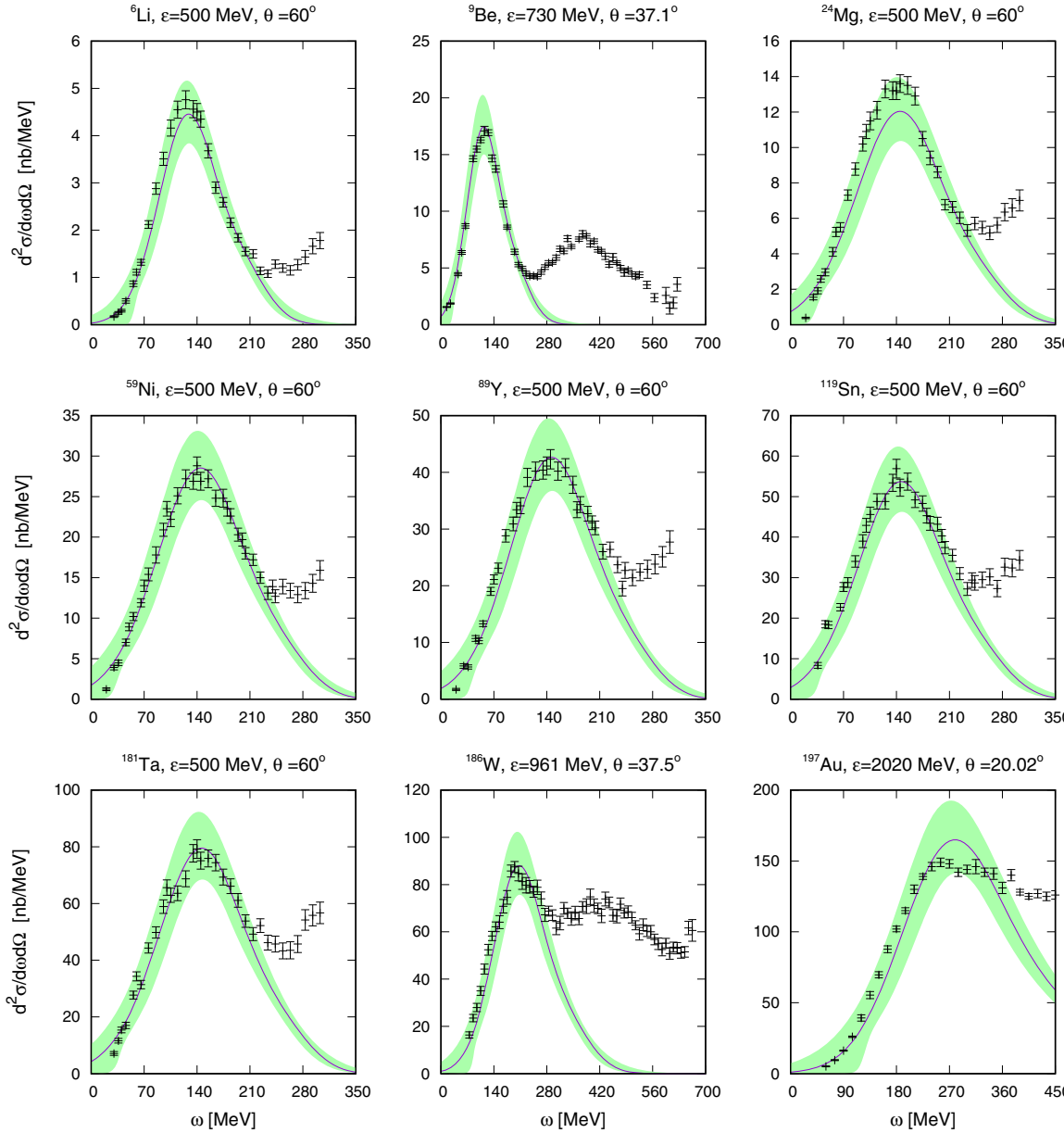

FIG. 11. Inclusive (e, e') cross-section data for nine different nuclei for different kinematics compared to the SuSAM* model as a function of energy transfer. Data are from Refs. [49–51].

points that collapse inside band C in Fig. 5 is more than 9 000 of the total ≈20 000 data.

IV. CROSS-SECTION RESULTS

In this section we use the phenomenological scaling function of Eq. (23) and the parameters corresponding to band B of Table I, to compute the (e, e') cross section, using the Fermi momenta and effective masses of columns 6 and 7 of Table II. The SuSAM* model predicts a central cross section inside a theoretical uncertainty band. The width of the cross-section band is related to the width of our parameterized scaling function for band B. Note that in the cross section the absolute value of the band width depends on the kinematics and on the nuclear species. This is because the cross section is obtained from the scaling function by multiplication by a kinematic-dependent function. Our cross-section results are here compared to experimental data for the 21 nuclei included in our fit. This comparison with the SuSAM* model has only been done before for the case of ^{12}C [43] and ^{16}O [45]. We also make comparisons with the new data for ^{48}Ti and ^{12}C performed in a recent experiment at JLab [52] and provide predictions for the ^{40}Ar nucleus corresponding to the kinematics of interest for the JLab experiment, that plans to extract the Argon spectral function.

The present results have also been studied by using bands A and C and parameters k_F, M^* from the different fits described in the last section. The global behavior of the result and the conclusions of this work are roughly preserved by using any of the three parameterized scaling functions and bands.

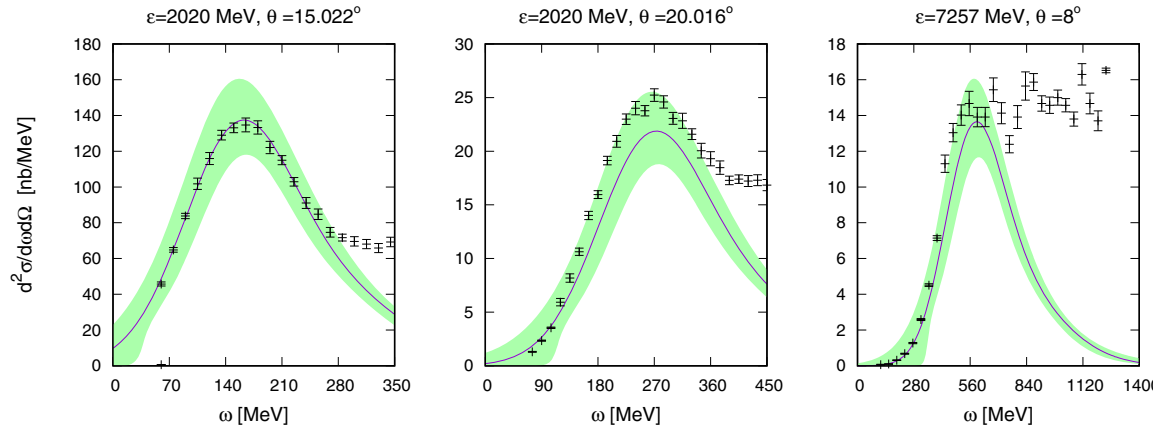

FIG. 12. Inclusive (e, e') cross-section data for ^{27}Al for selected kinematics compared to the SuSAM* model as a function of energy transfer. Data are from Refs. [49–51].

In Figs. 6–17 we show the predictions of our model for the (e, e') cross section compared to selected experimental data for each nucleus in the database, from ^{2}H to ^{238}U. The global description is quite acceptable given the simplicity of the SuSAM* model. A large subset of data fall inside the uncertainty band. In fact, most of the data used to perform the fit are inside our prediction bands by construction. The data that lie outside our prediction bands are typically those in the inelastic or deep region and those corresponding to low momentum transfer, and therefore breaking ψ^*-scaling because they fall outside the quasielastic region defined in Fig. 1. Alternatively, intermediate energy QE data falling outside our bands may indicate the existence of nuclear effects beyond the impulse approximation such as meson-exchange currents (MEC) or breaking the factorization approximation, like strong final state interactions.

In what follows we discuss in some detail the cross-section description for every single nucleus considered in our study.

A. The nucleus ^{2}H

The lighter nucleus considered in the fit corresponds to ^{2}H, shown in Fig. 6. We use the χ^2 fit values from Table II for the Fermi momentum, $k_F = 82$ MeV/c, and effective mass $M^* = 1$. The fact that the SuSAM*—based on the Fermi gas equations—reproduces a large fraction of deuterium data could seem shocking. But what our results reflect is that the deuterium quasielastic cross section is compatible with a momentum distribution of moderate extension, $k_F \approx 82$ MeV/c. This behavior dominates around the quasielastic region $-1 < \psi^* < 1$, while we in general subestimate the left tail of the cross section, corresponding to $\psi^* < -1$, and is related to PN short range correlations.

B. The nuclei ^{3}H and ^{3}He

The $A = 3$ light nuclei analyzed, ^{3}H and ^{3}He, are shown in Figs. 7 and 8, respectively. They are even better described than ^{2}H, with slightly different Fermi momenta, $k_F = 136$ and 130 MeV/c for H and He, respectively. The effective mass takes the same value $M^* = 0.98$ for both nuclei. The value of the Fermi momentum differ from the other fits, see Table II, ranging between 120 and 140 MeV/c. All these values of k_F give qualitatively similar predictions for the cross section, because the cross-section dependence on k_F is mild in a small momentum interval. The dependence on M^* is found to be stronger. However, note that the differences between the adjusted parameters for these nuclei can also be related to the different number of experimental data, which is much larger for the case of ^{3}He than for ^{3}H.

C. The nucleus ^{4}He

The ^{4}He nucleus is the nucleus with more quasielastic data in the database and is one with the better scaling properties. Selected cross-section predictions are shown in Fig. 9, computed with $k_F = 180$ MeV/c and $M^* = 0.86$, although equally good results can be obtained with $k_F = 160$ MeV/c and $M^* = 0.9$. Comparing with the cases $A = 2, 3$ we clearly see that the Fermi momentum increases with A, and the effective mass decreases with A. The QE cross-section description is quite good for many kinematics. It is remarkable that, given its simplicity, for intermediate energy the SuSAM* model seems to be as good as the more recent *ab initio* calculations [58] with relativistic corrections. In our view, this is so because the main dynamical ingredients of the QE processes are embedded into our model via the connection between relativity and effective mass.

D. The nucleus ^{12}C

Results for ^{12}C are shown in Fig. 10. We use $k_F = 217$ MeV/c and $M^* = 0.8$. Note that the SuSAM* model was first introduced in Ref. [43], where a comparison with all ^{12}C data was provided using band A of Table I and $k_F = 225$ MeV/c. This value of the Fermi momentum was obtained with a visual fit. In this work we have upgraded this description using band B, which incorporates a better description for low energy. But in general both descriptions are globally of the same quality around the QE peak. This nucleus is, together with ^{4}He, one of the better described nuclei taking into account the high number of data existing in the data base, ≈2800 each of them.

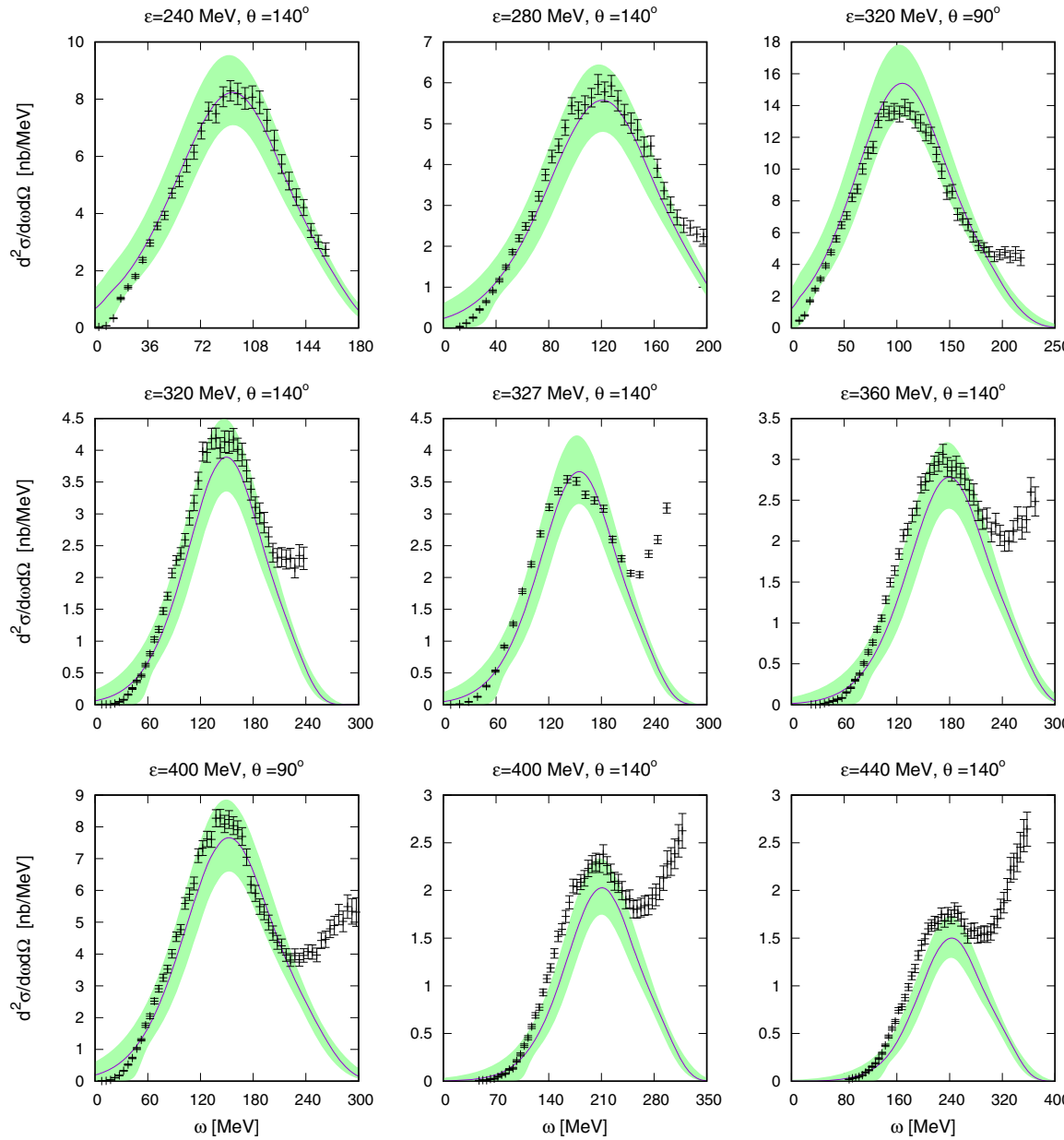

FIG. 13. Inclusive (e, e') cross-section data for ^{40}Ca for selected kinematics compared to the SuSAM* model as a function of energy transfer. Data are from Refs. [49–51].

E. The nuclei ^{6}Li, ^{9}Be, ^{24}Mg, ^{59}Ni, ^{89}Y, ^{119}Sn, ^{181}Ta, ^{186}W, and ^{197}Au

For these nuclei there are only a few set of kinematics available in the database, usually ≈20–40 QE data points only. Therefore, it is not possible to determine the parameters with high precision by maximizing the number of points inside the band, because there are many arrangements of the data points compatible with the theoretical band. For this same reason the χ^2 fit to each nuclei usually provides a good description of the experimental data for intermediate energy kinematics, where the scaling approach works better. This is shown in Fig. 11 with the parameters k_F and M^* taken from columns 6 and 7 of Table II. The QE data from Li to Au all fall with our band and are in general well described by the central value, with the exception of Mg and Au, which are slightly underestimated and overestimated at the peak position, respectively.

F. The nucleus ^{16}O

There are only a limited number of kinematics available for ^{16}O. However, they are enough for performing all the fits, with a good global description of data. We obtain $k_F = 250$ MeV/c in the χ^2 fit and $M^* = 0.79$. In the global and visual fit the Fermi momentum is more similar to that of ^{12}C. The comparison of band B with the experimental (e, e') cross section was shown in Fig. 1 of Ref. [45], where the SuSAM* parameters were first extracted for this nucleus, to apply the SuSAM* model

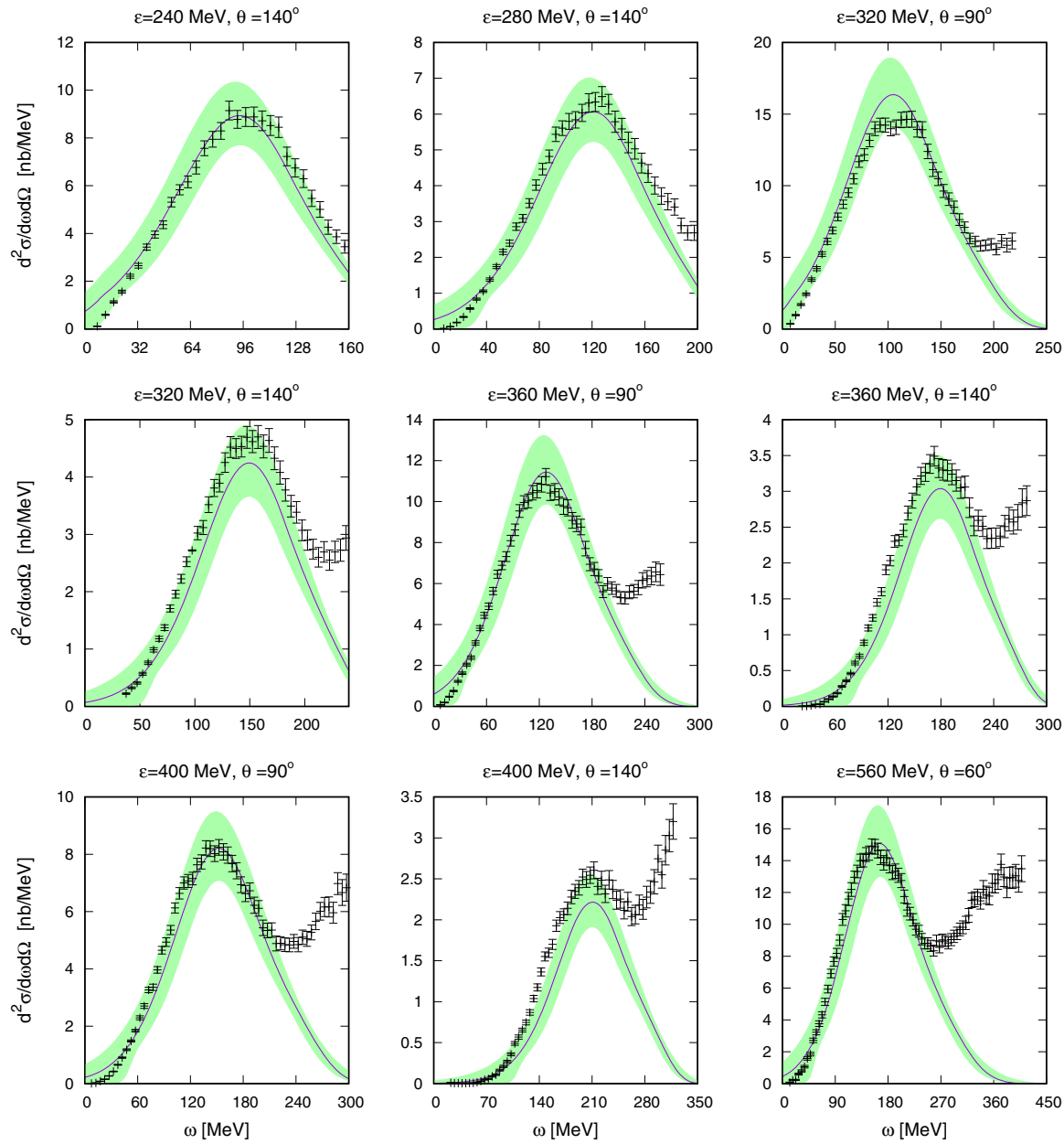

FIG. 14. Inclusive (e, e') cross-section data for ^{48}Ca for selected kinematics compared to the SuSAM* model as a function of energy transfer. Data are from Refs. [49–51].

to neutrino scattering on water, of interest for the recent T2K experiment [12]. More experimental kinematics for the (e, e') reaction on ^{16}O would be needed to reduce the uncertainty of the SuSAM* parameters.

G. The nucleus ^{27}Al

A number of ≈100 QE-like data are available for ^{27}Al in the data base. We show three kinematic sets in Fig. 12. This allows to extract $k_F = 249$ MeV/c and $M^* = 0.8$ in the χ^2 fit. Even with so limited number of data, it is also possible to extract these values by maximizing the number of points inside the band, obtaining similar values $k_F = 258$ MeV/c and $M^* = 0.78$. In the global fit the Fermi momentum is slightly reduced to 233 MeV/c, similar to the visual fit value.

H. The nuclei ^{40}Ca and ^{48}Ca

More abundant sets of data are available for the calcium isotopes ^{40}Ca and ^{48}Ca, with very similar values of Fermi momenta $k_F \approx 236$ MeV/c in the χ^2 fit and $M^* = 0.8$. In general, these nuclei are well described by the SuSAM* band for intermediate energies as shown in the selected kinematics of Figs. 13 and 14. The number of points inside the cross-section bands amount to 616 and 728, for slightly larger values of $k_F =$ 250 and 242 MeV/c, respectively, and $M^* = 0.73$ and 0.75.

I. The nucleus ^{56}Fe

Iron is an important case of study for some of the neutrino oscillation ongoing or planned experiments. In addition, this

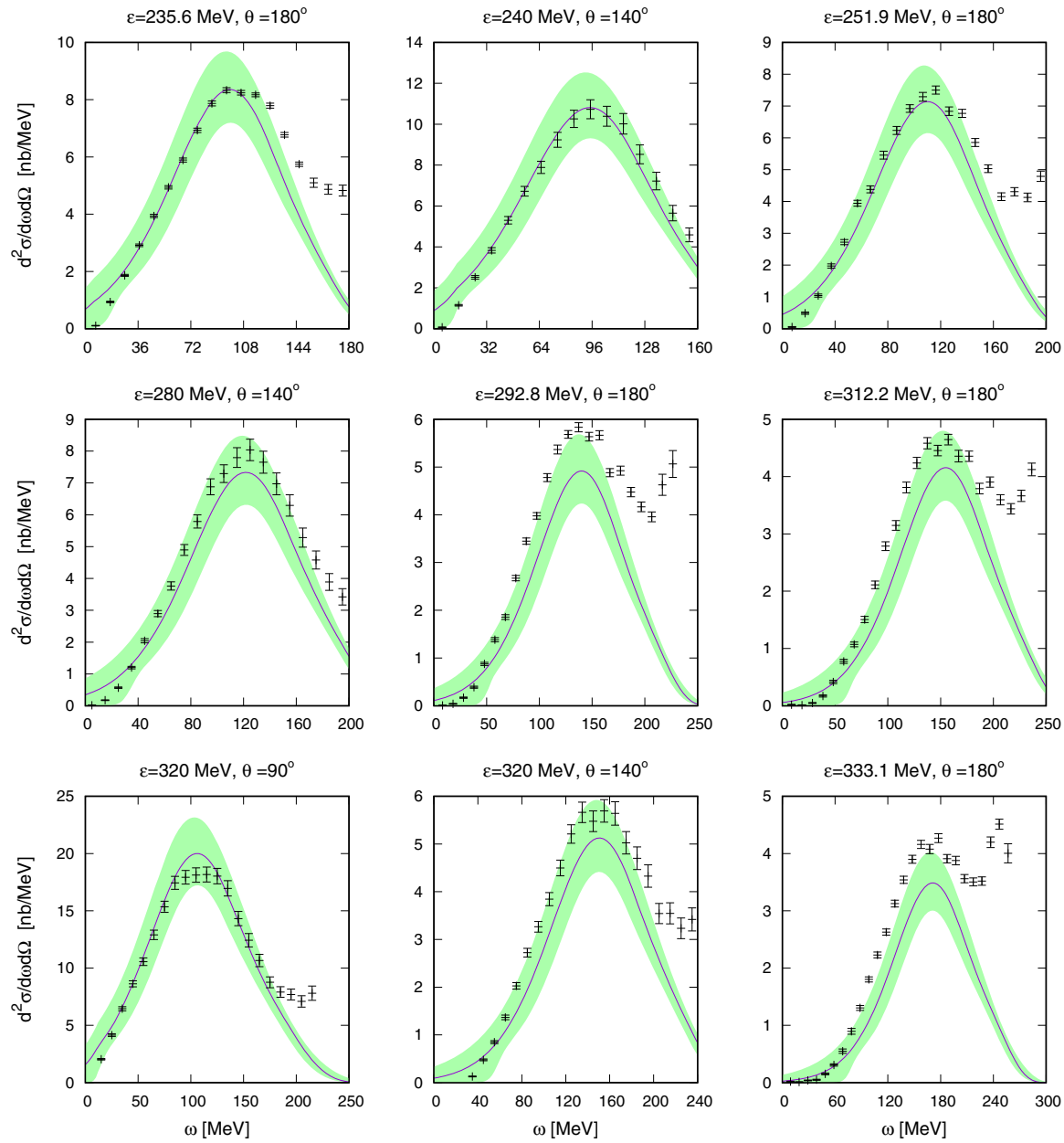

FIG. 15. Inclusive (e, e') cross-section data for ^{56}Fe for selected kinematics compared to the SuSAM* model as a function of energy transfer. Data are from Refs. [49–51].

is another nice example with abundant electron scattering experimental data for intermediate energy and this allows a precise determination of $k_F \approx 240$ MeV/c and $M^* \approx 0.7$. Cross-section results for this nucleus are shown in Fig. 15. A fair description of the data is obtained for incident energies $\epsilon < 2$ GeV.

J. The nucleus ^{208}Pb

For heavy nuclei the SuSAM* description is still possible even if the model is based on the factorization of a single nucleon cross section, which is expected to be violated by a strong final-state interaction (FSI) on nuclei such as ^{208}Pb, shown in Fig. 16. An indication is that the value of $\chi^2/N_{\rm QE}$, given in the last column of Table II, is bigger than one for all the heavy nuclei with abundant number of data. In particular, for lead, $\chi^2/N_{\rm QE} = 1.223$. This fit provides a Fermi momentum $k_F = 233$ MeV/c, similar to the values obtained for other medium/light nuclei, and effective mass $M^* = 0.56$. The other fits performed give rather similar numbers for these parameters. We have tried to include Coulomb corrections for this nucleus in terms of an effective momentum, but the results actually worsen. Additional effects beyond the impulse approximation, mainly meson exchange currents, are expected to be especially important for this nucleus and should be investigated in more depth in the future.

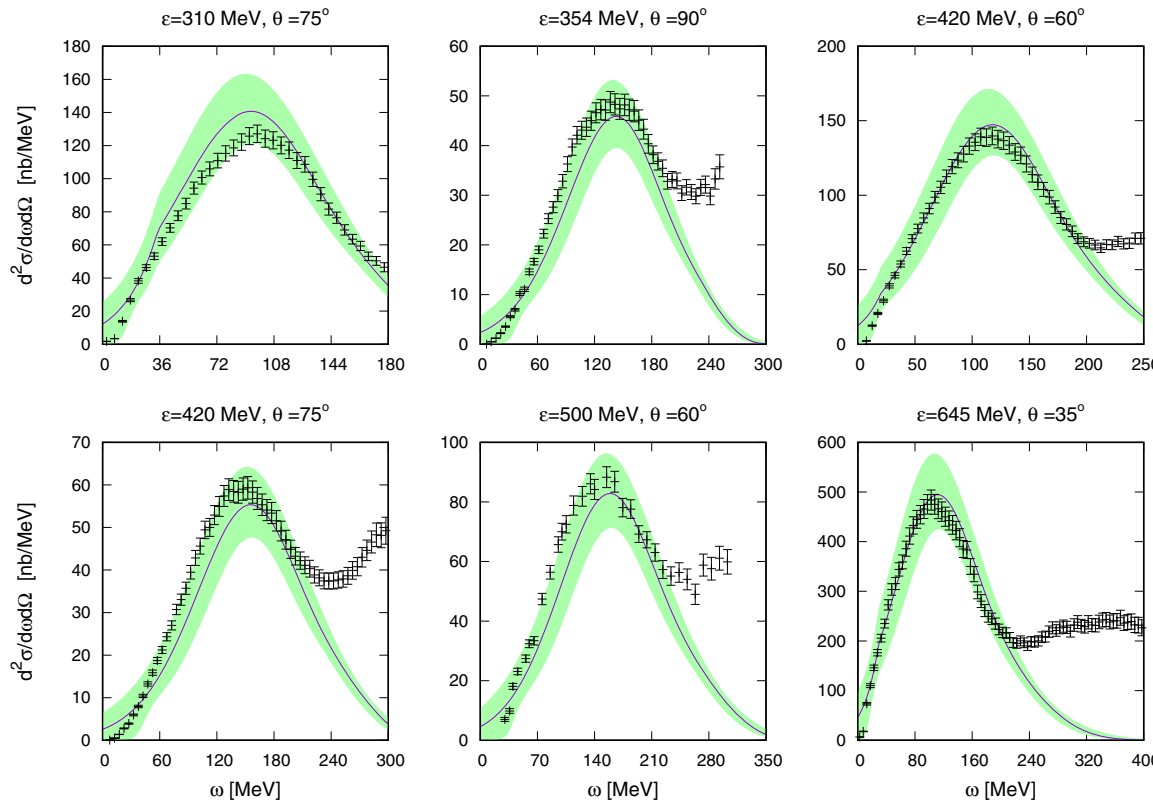

FIG. 16. Inclusive (e, e') cross-section data for ^{208}Pb for selected kinematics compared to the SuSAM* model as a function of energy transfer. Data are from Refs. [49–51].

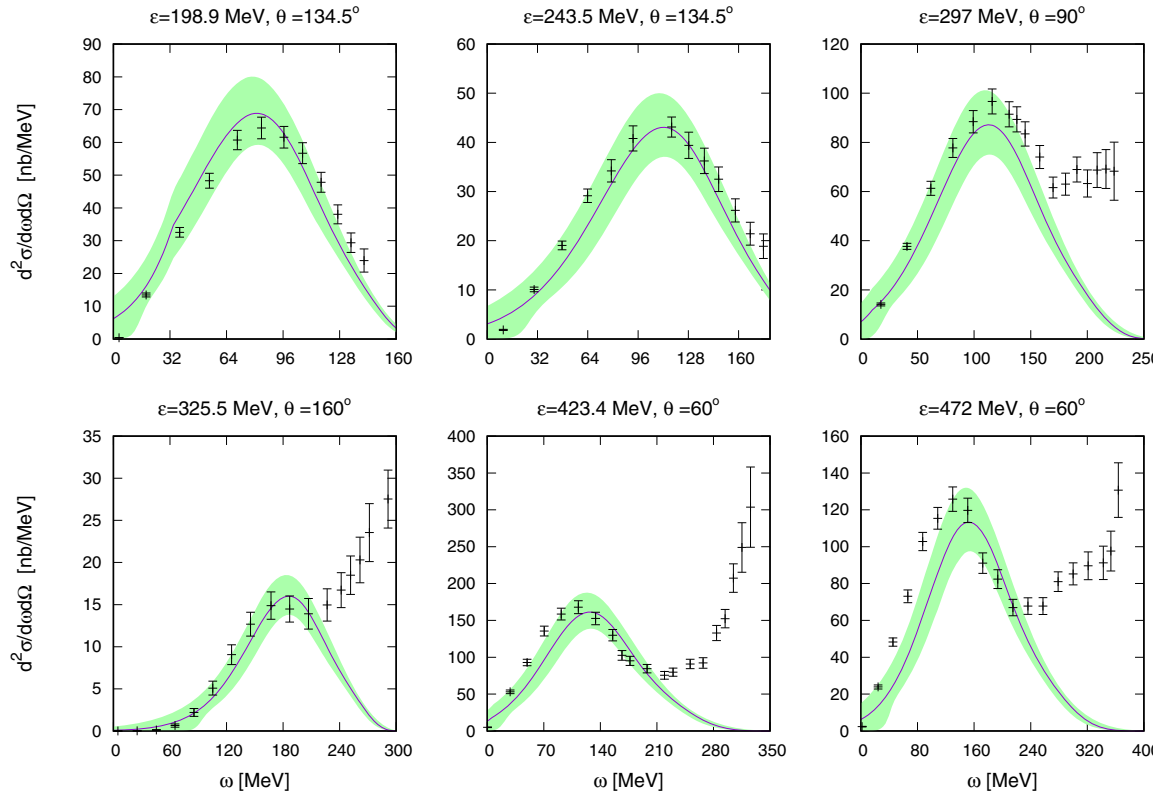

FIG. 17. Inclusive (e, e') cross-section data for ^{238}U for selected kinematics compared to the SuSAM* model as a function of energy transfer. Data are from Refs. [49–51].

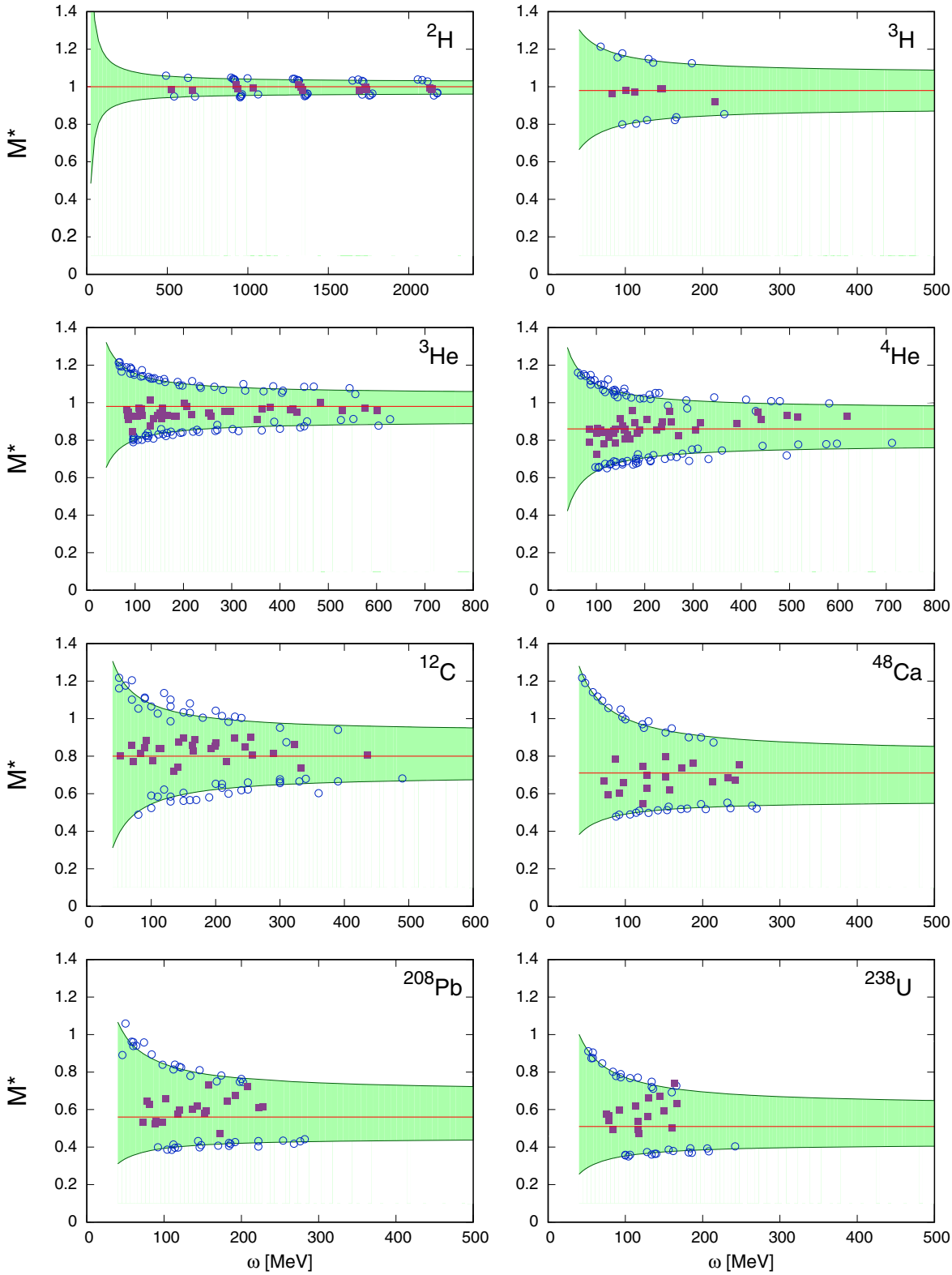

FIG. 18. Relativistic effective mass M^* computed from the QE peak position of the selected experimental data sets (violet squares) as a function of the energy transfer ω. The experimental bands for M^* have been obtained from the SuSAM* bands for the same experimental kinematics (circles) by computing the lower and upper limits for the effective mass allowed by the band.

K. The nucleus ^{238}U

Results for the heaviest nucleus analyzed, ^{238}U, are shown in Fig. 17. Even if the number of existent QE data is not so big as for lead, the description of this nucleus is the worst of all the nuclei analyzed. The $\chi^2/N_{\rm QE} = 1.74$ is the largest appearing in the last column of Table II, and the Fermi momentum obtained in the fit is surprisingly low $k_F = 219$ MeV/c, compared to lighter nuclei. Moreover in the global fit a very different value is obtained $k_F = 255$ MeV/c, closer to the expected value of nuclear matter. This again indicates that for heavy nuclei strong effects breaking the impulse approximation and the superscaling hypothesis should play an important role in the QE regime.

L. M^* uncertainty

In the previous results we have assumed that the effective mass is a constant parameter, which is determined by the position of the QE peak. While our parametrization of the scaling function in general describes well the position of the QE peak, we observe deviations for some kinematics. In fact, it is observed that for large Q^2 the QE peaks shows a shift to high energy. This is observed in particular, for ^{4}He when $\omega > 300$ MeV. One could try to improve the description by using a different "optimal" effective mass for each kinematics. In Fig. 18 we show this "optimal" effective mass computed for eight nuclei for each experimental kinematic set. Each set is defined by fixed incident electron energy and scattering angle. This effective mass is plotted as a function of ω at the QE peak. The optimal effective mass has been computed from the maximum of the experimental cross section by imposing the quasielastic condition

$$\omega = \frac{|Q^2|}{2m_N^*}, \tag{27}$$

from where

$$M^* = \frac{1}{m_N}\left(\frac{|Q^2|}{2\omega}\right)_{\rm max}. \tag{28}$$

This allows us to estimate a theoretical uncertainty in the effective mass obtained from the SuSAM* bands by this method, shown as the blue circles defining the borders of the green uncertainty band in Fig. 18. The circles in Fig. 18 have been obtained for each experimental kinematics from our cross-section prediction by the method displayed for example in Fig. 19 for a kinematics in ^{48}Ca. The method we used is as follows. We first draw the horizontal segment crossing the maximum of the central cross section. Then, we compute the two points P_u and P_d at the upper border of the band. These points are an estimation of the minimum and maximum ω position of the theoretical QE peak allowed by our band. From these two ω_u and ω_d we compute the up, M_u^*, and down, M_d^*, values of the effective mass by Eq. (28). This gives us the two values of the "optimal" effective mass shown in the bottom panel of Fig. 19, each one at a different ω position, ω_u and ω_d, respectively. Repeating this procedure for each experimental kinematics, we have obtained the blue circles in Fig. 18. Finally, to obtain the green bands defining our estimation of the effective mass uncertainty by this procedure,

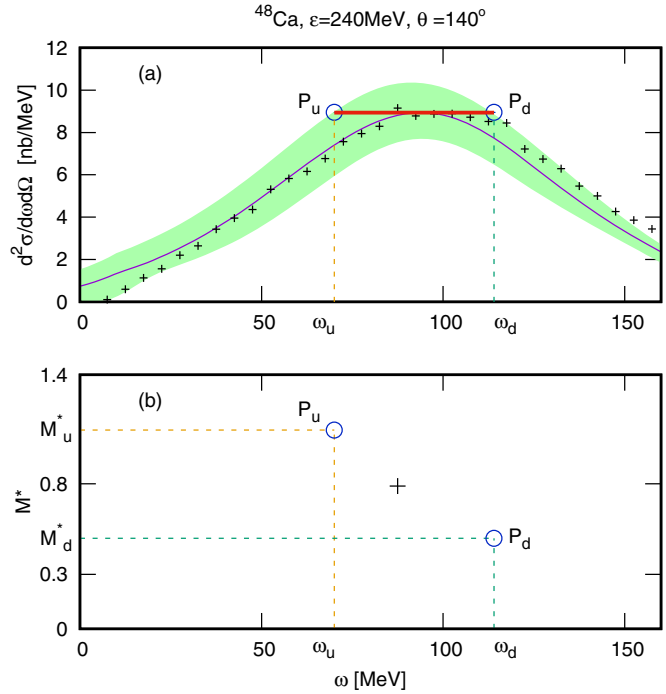

FIG. 19. Relativistic effective mass M^* computed from the QE peak position of the selected experimental data sets (squares) as a function of the energy transfer ω. The experimental bands for M^* have been obtained from the SuSAM* bands for the same experimental kinematics (blue circles) by computing the lower and upper limits for the effective mass allowed by the band.

we fit the borders of the band to the resulting points using the parametrization,

$$M^*_{u,d} = \frac{A_{u,d}}{\omega} + B_{u,d}. \tag{29}$$

An estimation of the uncertainty in M^* can be obtained for $\omega \to \infty$ as

$$\Delta M^* = \frac{B_u - B_d}{2}. \tag{30}$$

The values of the parameters $A_{u,d}$, $B_{u,d}$, and ΔM^* are given in Table IV. Their values amount roughly to $\approx$0.1 except for deuterium. The uncertainties in the effective mass are larger for heavier nuclei.

M. Predictions for ^{48}Ti and ^{40}Ar

In Ref. [52] the first measurement of the ^{48}Ti(e, e') cross section at Jefferson Lab was reported. The beam energy is $E = 2.222$ GeV and electron scattering angle $\theta = 15.541^\circ$ over a broad range of energy transfer. The purpose of this experiment was to obtain accurate quasielastic cross-section data for the nuclei Ti ($Z = 22$) and Ar ($N = 22$) to extract information needed for the neutrino experiments. In the electron scattering experiment the cross section of ^{12}C for the same kinematics was also measured for calibration. These data are compared with the SuSAM* model in Fig. 20. In the upper panels we show our predictions using the parameter values from the previous fit, i.e., $k_F \approx 217$ MeV/c for $A = 12$ and $k_F \approx 240$ MeV/c

TABLE IV. Parameters of the effective mass bands for different nuclei. The up and down coefficients are shown in columns 2 to 5. The theoretical errors ΔM^* of column 6 correspond to the $\omega \to \infty$ limit.

Nucleus	A_u (MeV)	B_u	A_d (MeV)	B_d	ΔM^*
^{2}H	15.984	1.024	− 11.655	0.965	0.03
^{3}H	9.377	1.07	− 8.94	0.888	0.09
^{3}He	11.06	1.045	− 9.85	0.9	0.07
^{4}He	13.133	0.967	− 14.202	0.777	0.1
^{12}C	15.236	0.925	− 15.562	0.700	0.11
^{27}Al	23.636	0.989	− 15.044	0.735	0.13
^{40}Ca	18.241	0.816	− 6.374	0.556	0.13
^{48}Ca	18.618	0.815	− 7.247	0.563	0.13
^{56}Fe	19.57	0.828	− 12.014	0.598	0.12
^{208}Pb	14.952	0.693	− 5.495	0.448	0.12
^{238}U	15.316	0.618	− 6.479	0.418	0.1

for $A = 48$, and $M^* = 0.8$ for both nuclei. We observe that our central prediction is slightly shifted towards high energy transfer with respect to the data for both nuclei. This means that for this particular kinematics a higher value for the effective mass is favored. In fact, the ^{12}C data are better described using $M^* = 0.9$, and ^{48}Ti needs $M^* = 0.85$ (see lower panels of Fig. 20). This is related again to the fact that the RMF model with a constant effective mass starts to fail for high momentum transfer, favoring an energy dependence of the effective mass, as mentioned in the previous subsection. The values of Fermi momenta are similar to those used in the analysis performed in Ref. [52] for this kinematics.

To finish we show in the last column of Fig. 20 our predictions for the ^{40}Ar(e, e') quasielastic cross section for the same kinematics, of interest for the new experiments being performed at JLab [52,59,60]. For argon we show our band prediction for $k_F = 240$ MeV/c and for two possible values of the effective mass for this kinematics, $M^* = 0.8$ and 0.85. The knowledge of the experimental cross section for this kinematics would be useful in our formalism to extract the precise value of the effective mass, needed to describe the neutrino cross section for the same kinematics. Note that, in the previous experiment on Ar [61,62], the momentum transfer is too low for a reasonable simultaneous extraction of the effective mass and the Fermi momentum with our formalism.

V. CONCLUSIONS

In this paper we have analyzed the world data of inclusive quasielastic electron scattering within the SuSAM* model. This is an alternative scaling approach based on the relativistic mean-field model of nuclear matter instead of the more usual noninteracting relativistic Fermi gas. The new scaling variable ψ^* thus incorporates dynamical ingredients through the relativistic effective mass M^*, which emerges from the scalar and vector potentials in the Walecka model. We have applied several methods to obtain a phenomenological scaling function $f^*(\psi^*)$ from the inclusive (e, e') reaction data. Our procedure is to start from a scaling function extracted from

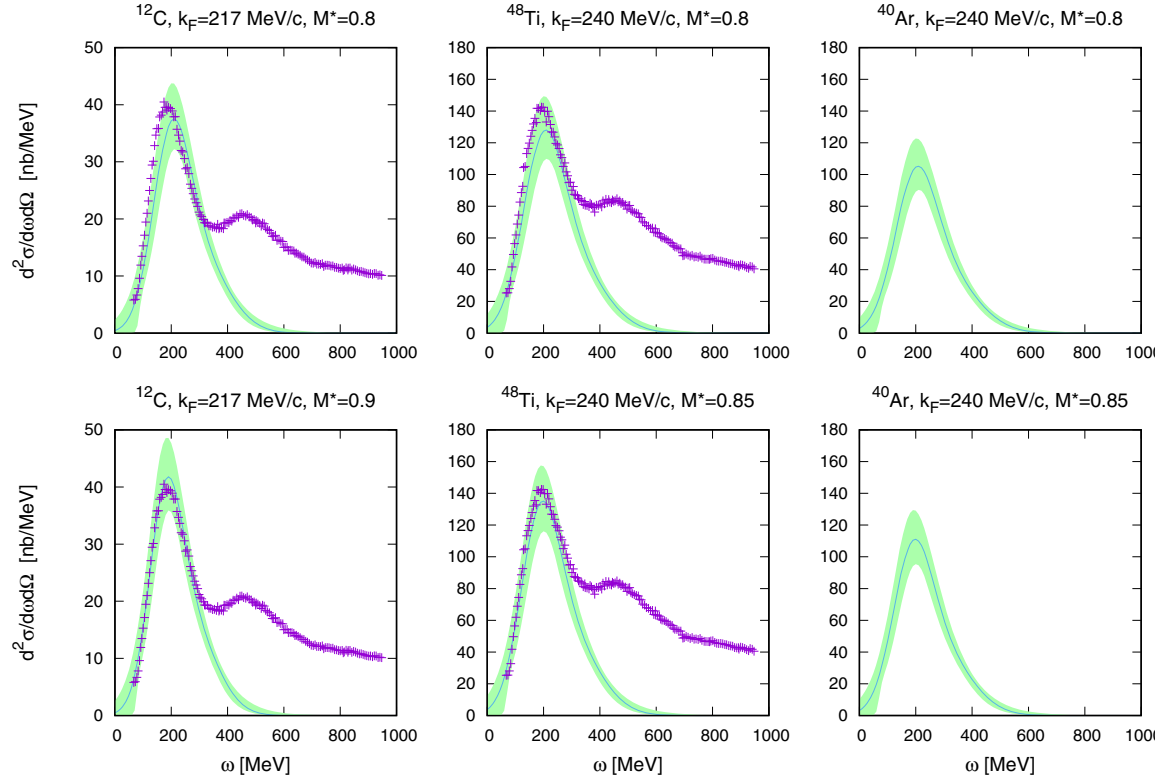

FIG. 20. Inclusive (e, e') cross sections of ^{12}C, ^{48}Ti, and ^{40}Ar for the kinematics $\epsilon = 2222$ MeV, $\theta = 15.541^{\circ}$, of the recent JLab experiment [52], compared to the SuSAM* model as a function of energy transfer.

^{12}C data as initial guess and use it to extract the effective mass and Fermi momentum of the remaining nuclei. In this work we have checked that this method is consistent with performing a global fit of the scaling function and all the parameters k_F, M^* over the full database for 21 nuclei.

Thus, superscaling has been shown to be valid for a large body of the (e, e') data, because the experimental scaling function $f^*(\psi^*)$ collapses into a thick band that here has been parameterized with combinations of simple Gaussian functions. This unique function allows to describe the intermediate energy QE cross section for light to heavy nuclei, from ^{2}H to ^{238}U, with tabulated values of k_F and M^*. Our fit has also allowed us to estimate the error in the extracted parameters $\Delta k_F \approx 10\,\mathrm{MeV/c}$ and $\Delta M^* \approx 0.1$.

Three similar parametrizations, A, B, C, of the phenomenological scaling function $f^*(\psi^*)$ and uncertainty band have been tabulated. With these we have presented a systematic analysis of the predicted QE cross sections and uncertainties compared to the data. We observe that the uncertainty band thickness depends on the kinematics. More than 9 000 data of the total 20 000 data are found to be "quasielastic" as they fall inside the uncertainty band. The present results have been shown using band B, but they have also been studied by using bands A and C and parameters k_F, M^* from the different fits. The global results and the conclusions of this work are preserved against these alternative parameterizations.

Our model provides one of the best global descriptions of QE data with a single nuclear model. The success is due not only because its parameters have been obtained by fitting the inclusive cross section directly. One crucial reason for the good results is because our model contains by construction the enhancement of the transverse components of the electromagnetic current. This is due to the dynamical enhancement of the lower components of the Dirac spinors by effect of the relativistic effective mass in nuclei, which is lighter than in free space.

Note that this enhancement of the transverse response is not observed in the nuclear isoscalar magnetic moments because there is a cancellation with the RPA corrections in the σ-ω model for low energy and momentum transfers [63]. These RPA-type vertex corrections were found to reduce the form factors for $q < 1\ \mathrm{fm}^{-1} \simeq 200\,\mathrm{MeV/c}$, but gave rise to an enhancement for larger q [64]. This is consistent with the assumed fact that the RPA corrections are small for high q. Since our description of the (e, e') reaction is focused for large $q \geqslant 2k_F$ at the QE peak, defined by $\omega = |Q^2|/2m_N^*$, the quasifree processes are dominant and collective excitations are expected to play a minor role.

Our model only requires the assumptions of gauge invariance, relativity, and scaling, which determines the values of the relativistic effective mass and the Fermi momentum. The model is blind to the sorts of nuclear effects involved in the quasielastic interaction, which are encoded into the scaling function $f^*(\psi^*)$ and its uncertainty band. Whatever nuclear effect which breaks the impulse approximation or the factorization of the cross section on which scaling is based, is included only on the average. These may include MEC and FSI as more direct candidates, but also short-range correlations, which should be more important for negative values of the scaling variable $\psi^* < -1$, out of the range of the fit made here. These very same effects probably give rise to many of the experimental data falling outside our bands. In future work we expect to reduce the band thickness adding to the scaling model a contribution from MEC in the 2p-2h channel, which explicitly accounts for specific scaling violations.

Our scaling function parametrization also provides a simple test for theoretical studies, which should fall inside the SuSAM* uncertainty band. The universality of the scaling function allows this model to be extended to provide tight constraints in quasielastic neutrino scattering for a wide variety of targets. In particular, we have provided predictions for the (e, e') cross section of Argon, of interest to current and upcoming neutrino experiments.

ACKNOWLEDGMENTS

This work has been partially supported by the Spanish Ministerio de Economia y Competitividad (Grants No. FIS2014-59386-P and No. FIS2017-85053-C2-1-P) and by the Junta de Andalucia (Grant No. FQM-225). V.L.M.C. acknowledges a contract with Universidad de Granada funded by the Junta de Andalucia (Spain) and by the European Social Fund.

[1] U. Mosel, Ann. Rev. Nuc. Part. Sci. **66**, 171 (2016).
[2] T. Katori and M. Martini, J. Phys. G **45**, 013001 (2018).
[3] L. Alvarez-Ruso, Y. Hayato, and J. Nieves, New J. Phys. **16**, 075015 (2014).
[4] A. M. Ankowski and C. Mariani, J. Phys. G **44**, 054001 (2017).
[5] O. Benhar, P. Huber, C. Mariani, and D. Meloni, Phys. Rep. **700**, 1 (2017).
[6] V. Lyubushkin *et al.* (NOMAD Collaboration), Eur. Phys. J. C **63**, 355 (2009).
[7] A. Aguilar-Arevalo *et al.* (MiniBooNE Collaboration), Phys. Rev. D **81**, 092005 (2010).
[8] A. Aguilar-Arevalo *et al.* (MiniBooNE Collaboration), Phys. Rev. D **88**, 032001 (2013).
[9] G. A. Fiorentini (MINERvA Collaboration) Phys. Rev. Lett. **111**, 022502 (2013).
[10] K. Abe *et al.* (T2K Collaboration), Phys. Rev. D **87**, 092003 (2013).
[11] K. Abe *et al.* (T2K Collaboration), Phys. Rev. D **93**, 112012 (2016).
[12] K. Abe *et al.* (T2K Collaboration), Phys. Rev. D **97**, 012001 (2018).
[13] M. Martini, M. Ericson, G. Chanfray, and J. Marteau, Phys. Rev. C **80**, 065501 (2009).
[14] J. Nieves, I. R. Simo, and M. J. Vicente Vacas, Phys. Rev. C **83**, 045501 (2011).
[15] K. Gallmeister, U. Mosel, and J. Weil, Phys. Rev. C **94**, 035502 (2016).
[16] G. D. Megias, J. E. Amaro, M. B. Barbaro, J. A. Caballero, T. W. Donnelly, and I. R. Simo, Phys. Rev. D **94**, 093004 (2016).

[17] G. D. Megias, M. V. Ivanov, R. Gonzalez-Jimenez, M. B. Barbaro, J. A. Caballero, T. W. Donnelly, and J. M. Udias, Phys. Rev. D **89**, 093002 (2014); **91**, 039903(E) (2015).
[18] A. M. Ankowski, Phys. Rev. D **92**, 013007 (2015).
[19] R. Gran, J. Nieves, F. Sanchez, and M. J. Vicente Vacas, Phys. Rev. D **88**, 113007 (2013).
[20] V. Pandey, N. Jachowicz, M. Martini, R. Gonzalez-Jimenez, J. Ryckebusch, T. Van Cuyck, and N. Van Dessel, Phys. Rev. C **94**, 054609 (2016).
[21] M. Martini, N. Jachowicz, M. Ericson, V. Pandey, T. Van Cuyck, and N. Van Dessel, Phys. Rev. C **94**, 015501 (2016).
[22] A. Lovato, S. Gandolfi, J. Carlson, Steven C. Pieper, and R. Schiavilla, Phys. Rev. Lett. **117**, 082501 (2016).
[23] V. Pandey, N. Jachowicz, T. Van Cuyck, J. Ryckebusch, and M. Martini, Phys. Rev. C **92**, 024606 (2015).
[24] A. M. Ankowski, O. Benhar, and M. Sakuda, Phys. Rev. D **91**, 033005 (2015).
[25] N. Rocco, A. Lovato, and O. Benhar, Phys. Rev. Lett. **116**, 192501 (2016).
[26] J. E. Amaro, M. B. Barbaro, J. A. Caballero, T. W. Donnelly, and A. Molinari, Phys. Rep. **368**, 317 (2002).
[27] J. E. Amaro, M. B. Barbaro, J. A. Caballero, T. W. Donnelly, and C. Maieron, Phys. Rev. C **71**, 065501 (2005).
[28] J. A. Caballero, J. E. Amaro, M. B. Barbaro, T. W. Donnelly, and J. M. Udias, Phys. Lett. B **653**, 366 (2007).
[29] J. M. Udias, J. A. Caballero, E. Moya de Guerra, J. E. Amaro and T. W. Donnelly, Phys. Rev. Lett. **83**, 5451 (1999).
[30] A. Bodek, M. E. Christy, and B. Coopersmith, Eur. Phys. J. C **74**, 3091 (2014).
[31] A. Gil, J. Nieves, and E. Oset, Nucl. Phys. A **627**, 543 (1997).
[32] I. R. Simo, J. E. Amaro, M. B. Barbaro, A. De Pace, J. A. Caballero, and T. W. Donnelly, J. Phys. G **44**, 065105 (2017).
[33] J. Nieves and J. E. Sobczyk, Ann. Phys. **383**, 455 (2017).
[34] W. M. Alberico, A. Molinari, T. W. Donnelly, E. L. Kronenberg, and J. W. Van Orden, Phys Rev. C **38**, 1801 (1988).
[35] T. W. Donnelly and I. Sick, Phys. Rev. Lett. **82**, 3212 (1999).
[36] T. W. Donnelly and I. Sick, Phys. Rev. C **60**, 065502 (1999).
[37] C. Maieron, T. W. Donnelly, and I. Sick, Phys. Rev. C **65**, 025502 (2002).
[38] J. E. Amaro, M. B. Barbaro, J. A. Caballero, T. W. Donnelly, A. Molinari, and I. Sick, Phys. Rev. C **71**, 015501 (2005).
[39] C. J. Horowitz, D. P. Murdock, and B. D. Serot, in *Computational Nuclear Physics*, Vol. 1 (Springer-Verlag, Berlin, 1991).
[40] R. Gonzalez-Jimenez, G. D. Megias, M. B. Barbaro, J. A. Caballero, and T. W. Donnelly, Phys. Rev. C **90**, 035501 (2014).
[41] G. D. Megias, J. E. Amaro, M. B. Barbaro, J. A. Caballero, and T. W. Donnelly, Phys. Rev. D **94**, 013012 (2016).
[42] J. E. Amaro, E. Ruiz Arriola, and I. R. Simo, Phys. Rev. C **92**, 054607 (2015).
[43] J. E. Amaro, E. Ruiz Arriola, and I. R. Simo, Phys. Rev. D **95**, 076009 (2017).
[44] V. L. Martinez-Consentino, I. R. Simo, J. E. Amaro, and E. Ruiz Arriola, Phys. Rev. C **96**, 064612 (2017).
[45] I. R. Simo, V. L. Martinez-Consentino, J. E. Amaro, and E. Ruiz Arriola, Phys. Rev. D **97**, 116006 (2018).
[46] R. Rosenfelder, Ann. Phys. (N. Y.) **128**, 188 (1980).
[47] B. D. Serot and J. D. Walecka, *The Relativistic Nuclear Many-Body Problem*, In Advance in Nuclear Physics, edited by J. W. Negele and E. Vogt (Plenum Press, New York, 1986), Vol. 16.
[48] K. Wehrberger, Phys. Rep. **225**, 273 (1993).
[49] O. Benhar, D. Day, and I. Sick, arXiv:nucl-ex/0603032.
[50] O. Benhar, D. Day, and I. Sick, http://faculty.virginia.edu/qes-archive/.
[51] O. Benhar, D. Day, and I. Sick, Rev. Mod. Phys. **80**, 189 (2008).
[52] H. Dai *et al.* (Jefferson Lab Hall A Collaboration), Phys. Rev. C **98**, 014617 (2018).
[53] M. B. Barbaro, R. Cenni, A. De Pace, T. W. Donnelly, and A. Molinari, Nucl. Phys. A **643**, 137 (1998).
[54] T. De Forest, Nucl. Phys. A **392**, 232 (1983).
[55] S. Galster, H. Klein, J. Moritz, K. H. Schmidt, D. Wegener, and J. Bleckwenn, Nucl. Phys. B **32**, 221 (1971).
[56] R. B. Wiringa, R. Schiavilla, S. C. Pieper, and J. Carlson, Phys. Rev. C **89**, 024305 (2014).
[57] I. R. Simo, R. N. Perez, J. E. Amaro, and E. Ruiz Arriola, Phys. Rev. C **95**, 054003 (2017).
[58] N. Rocco, W. Leidemann, A. Lovato, and G. Orlandini, Phys. Rev. C **97**, 055501 (2018).
[59] V. Pandey *et al.*, arXiv:1711.01671 [nucl-ex].
[60] O. Benhar *et al.*, arXiv:1406.4080 [nucl-ex].
[61] M. Anghinolfi *et al.*, J. Phys. G **21**, L9 (1995).
[62] A. M. Ankowski and J. T. Sobczyk, Phys. Rev. C **77**, 044311 (2008).
[63] S. Ichii, W. Bentz, A. Arima, and T. Suzuki, Phys. Lett. B **192**, 11 (1987).
[64] S. Ichii, W. Bentz, A. Arima, and T. Suzuki, Nucl. Phys. A **487**, 493 (1988).